Space Sci Rev (2020) 216:108
https://doi.org/10.1007/s11214-020-00731-5

SPECIAL COMMUNICATION

Hayabusa2's Superior Solar Conjunction Phase

Trajectory Design, Guidance and Navigation

Stefania Soldini[1,2] · **Tomohiro Yamaguchi**[2] ·
Yuichi Tsuda[2] · **Saiki Takanao**[2] · **Satoru Nakazawa**[2]

Received: 20 November 2019 / Accepted: 26 August 2020

Abstract Hayabusa2 is the ongoing JAXA's sample and return mission to the asteroid Ryugu. In late 2018, Ryugu was in superior solar conjunction with the Earth. It is the first time that a spacecraft experiences the blackouts in the communication link with the Earth while hovering around a small celestial body. In this article, the design of the nominal conjunction trajectory flown by the Hayabusa2's spacecraft is presented. The requirements for the conjunction trajectory were (1) to guarantee a low fuel consumption, (2) to ensure the visibility of the asteroid by the spacecraft's wide angle camera (60° FoV), and (3) to increase the spacecraft altitude to a safety location (~ 109 km) from the nominal BOX-A operation of 20 km (Home Position - HP). Finally, (4) to return at BOX-A after the conjunction phase. Given the mission constraints, the designed conjunction trajectory appears to have a fish-shape in the Hill coordinates therefore we renamed it as "ayu" (sweetfish in Japanese) trajectory. The optNEAR tool was developed for the guidance (ΔVs planning) and navigation design of the Hayabusa2's conjunction mission phase. A preliminary sensitivity analysis in the Hill reference frame proved that the ayu trajectory is a good candidate for the conjunction operation of hovering satellite. The solution in the Hill coordinates is refined in the full-body planetary dynamics (optNEAR Tool) before flight. The ayu conjunction trajectory requires (a) two deterministic ΔVs at the Conjunction Orbit Insertion (COI) point and at the Home-position Recovery Maneuver (HRM) point respectively. (b) Two stochastic ΔVs, known as Trajectory Correction Manoeuvres (TCMs), before and after the deep conjunction phase are also required. The constraint linear covariance analysis in the full-body dynamics is here derived and used for the preliminary guidance and navigation planning. The results of the covariance analysis were validated in a nonlinear sense with a Monte Carlo approach which proved the validity of the semi-analytic method for the stochastic ΔVs planning derived in this paper.

Note by the Editor: This is a Special Communication, linked to the Topical Volume on the Hayabusa2 mission published in Space Science Reviews (https://link.springer.com/journal/11214/208/1).

✉ S. Soldini
stefania.soldini@liverpool.ac.uk

[1] Department of Mechanical, Materials and Aerospace Engineering University of Liverpool, Liverpool, UK

[2] Institute of Space and Astronautical Science, JAXA, Sagamihara, Japan

Keywords Superior solar conjunction · Hayabusa2 · Ryugu · Hovering satellite · optNEAR tool

Acronyms

AOCS	Attitude Orbit Control System
COI	Conjunction Orbit Insertion
FD	Flight Dynamics
FoV	Field of View
HP	Home Position (20 km from Ryugu Asteroid)
HP-NAV	Home Position-NAVigation
HRM	Home-position Recovery Maneuver
OD	Orbit Determination
optNEAR	optimum trajectory Near Earth Asteroid Regions
RCS	Reaction Control System
SEP	Sun-Earth-Probe
SRP	Solar Radiation Pressure
TCM	Trajectory Control Maneuver
ToF	Time of Flight

1 Introduction

Hayabusa2 is the Japanese sample and return robotic mission to the Ryugu asteroid (Watanabe et al. 2019). On 27th of July 2018, the Hayabusa2 spacecraft arrived at Ryugu where the spacecraft-asteroid proximity operations have started. The spacecraft is designed to hover above Ryugu at a distance of 20 km, known as Home Position (HP). In early December 2018, the Hayabusa2 spacecraft was located behind the Sun as seen from the Earth. This condition is known as superior solar conjunction because of the solar radio interference constraints. During the solar conjunction the signal pass through the solar corona that causes a substantial increase in the Doppler data noise with consequent degradation in the orbit determination accuracy (Morley and Budnik 2007). The Earth, the Sun and Ryugu were almost aligned on the 11$^{\text{th}}$ of December 2018 by causing a temporary blackout in the communication link between the Hayabusa2 spacecraft and the Earth. The solar radio interference constraints for the Hayabusa2 spacecraft is the region within 3° of the Sun-Earth-Probe (SEP) angle called Solar Exclusion Zone (SEZ) (Canalias and Masdemont 2004). The superior solar conjunction event represents a challenge for hovering satellite as communications with the Earth are prohibited. During the Earth-Ryugu communication blackout, the spacecraft needed to be placed in a safe “conjunction” trajectory to prevent undesired: close approaches, escape dynamics or, in the worst case, collision with the asteroid.

Deep space missions’ vicinity operation techniques include (1) fly-bys (Taylor et al. 2017), (2) orbiting (i.e. OSIRIS-REx mission (Lauretta et al. 2017)) and (3) hovering (i.e. Hayabusa (Yoshikawa et al. 2013) and Hayabusa2 missions (Watanabe et al. 2017)).

(1) For spacecrafts in fly-by with the asteroid, the spacecraft orbit is designed in a heliocentric way and, usually, a manoeuvre is given to increase the Spacecraft-Asteroid relative distance (i.e. Rosetta mission) with respect to the Sun (Morabito et al. 2003).
(2) For a spacecraft in orbit around an asteroid, it is possible to either place the spacecraft in a stable orbit or design an orbit that naturally avoids the SEZ regions (i.e. Terminator Orbits (Takahashi and Scheeres 2019) and Halo Orbits (Farres et al. 2013).

(3) A spacecraft in hovering with the asteroid has the advantage to ease communication with the Earth through a relatively simple communication link geometry that is a fundamental asset for Touch-Down operations in deep space. However, the major disadvantage is that a spacecraft in hovering is located at a highly unstable condition and it requires to be artificially constrained at the HP altitude (of 20 km altitude) with daily maneuvers called BOX-A ($x_{hp} = y_{hp} = \pm 0.5$ km, $z_{hp} = 20 \pm 2.5$ km) operation for the Hayabusa2 mission. Therefore, the design of a low fuel expenditure conjunction manoeuvre for a hovering spacecraft is not straightforward as for the case of spacecrafts in (1) fly-by or (2) orbiting the asteroid.

The Hayabusa spacecraft experienced the solar conjunction during the heliocentric transfer phase before its arrival to the asteroid Itokawa, which is a common procedure for deep space missions (Yoshikawa et al. 2013). It is the first time that a spacecraft experiences the superior solar conjunction while in hovering. Thus, to the best of our knowledge, the solar conjunction phase for a hovering spacecraft has never been studied in the past.

In this article, a low energy transfer trajectory is proposed as a candidate of the conjunction trajectory for the Hayabusa2 spacecraft. The main idea here is to make use of the natural dynamics in the Asteroid-Sun system, knowing that in the Hill problem, the spacecraft motion towards the Sun direction can be forbidden by fixing the S/C energy. This approach is similar to ballistic captures (Qi et al. 2014), weak stability boundaries (Belbruno et al. 2010) or low energy transfers (Koon et al. 2001). JAXA's Hiten mission used similar ideas for the design of a recovery trajectory in the patched Circular Restricted Three-Body Problem (CR3BP) of the Sun-Earth and Earth-Moon system (Uesugi et al. 1991). This low energy trajectory aims at inserting the spacecraft in a trajectory towards the forbidden region of motion (known as curve of zero velocity) located at higher altitude with respect to the HP position. Once the spacecraft had reached the boundary of the curve of zero velocity on the 11th of December 2018, its velocity was naturally inverted in the opposite direction and the spacecraft returned at the HP point by decreasing its altitude. The conjunction orbit is designed in the Hill frame of the Sun-Asteroid system and due to its fish-shape was named "ayu" (sweetfish in Japanese). The time of flight of this trajectory is around 30 days and it requires two deterministic ΔVs. The first maneuver is given at the Conjunction Orbit Insertion (COI) point (Home Position before the conjunction, 23rd November 2018) and the second one at the Home-position Recovery Maneuver (HRM) point (Home Position after the conjunction, 29th December 2018) with a total expenditure in the ΔV less than 1 m/s which implies low fuel consumption. optNEAR (optimum trajectory in Near Earth Asteroid Regions) tool was developed for the trajectory, guidance navigation planning of the ayu conjunction trajectory as the JAXA's software JATOPS (Jaxa Approach Trajectory Optimizer with Statistical Constraints) developed for the Hayabusa2 approach phase could not determine the optimum conjunction solution following the required mission constraints.

The article is organised as follow: Sect. 2 provides an overview of the conjunction phase's mission planning and the relevant definitions of the reference frames used. The equations of motion are given in the Hill coordinates in Sect. 3. Section 4 presents the shooting method for the design of the ayu trajectory developed in the optNEAR tool. Section 5 shows the results of the uncertainty analysis in the deterministic maneuvers at COI and HRM. Section 6 investigates the effect of the navigation in BOX-A on the COI maneuvers while Sect. 7 shows the shooting method for the design of the TCM maneuvers. Finally, the results of the guidance and navigation design are presented in Sect. 8.

2 Overview of the Hayabusa2's Superior Solar conjunction Phase

For the ΔV planning of the ayu conjunction trajectory, the required interfaces between the Orbit Determination (OD), Flight Dynamics (FD), and the Attitude Orbit Control System (AOCS) teams were prepared. The OD team provides the inputs for the trajectory design to the Flight Dynamics (FD) team as the estimates of the spacecraft's state vector, and the initial knowledge of the covariance matrix (after the navigation). The AOCS team receives the product of the trajectory planning from the FD team in a "way" file ΔV sequence format. Different teams require the definition of the state vector of the spacecraft and of the ΔV in a specific reference system. At least four reference frames are required for the solar conjunction mission phase and their mutual rotations have to be derived. Figure 1 shows a schematic overview of the entire solar conjunction phase for the Hayabusa2 mission and of the four main reference frames used. Two main phases are identified here: the Mission Design and Mission Operation. Two reference frames are required for Mission Design as:

(1) The *Hill reference frame* is centered at Ryugu. In this system, the Sun occupies a fixed relative distance with Ryugu and it is always located in the x_{hill} negative coordinates. This reference frame is rotating along the z_{hill}-axis with an angular velocity equal to the Sun-Ryugu mean motion[1] with respect to the J2000EQ reference frame.

(2) The *J2000 equatorial reference frame* is here either centered at the Solar System Barycenter (SSB) (J2000EQ) or at Ryugu (J2000EQ-Ry), as shown in the blue dot square in Fig. 1. Note that the J2000EQ reference frame is an inertial reference frame centered in the SSB, while the axes of the J2000EQ-Ry reference frame are parallel to the J2000 EQuatorial (J2000EQ) frame but centered at Ryugu asteroid.

In this article, the Hill reference frame (1) is used for the design of the nominal trajectory as a 1st guess of the ephemeries dynamical system (2) (N-Body Problem) where the gravity of all planets, the Sun, the Moon and Ryugu are taken into account. The solution in the Hill system is refined with the developed N-Body propagator called *optNEAR* (*op*timum *t*rajectory in *N*ear *E*arth *A*steroid *R*egions). optNEAR is written in the J2000EQ-Ry reference frame and it makes use of the NASA's SPICE Toolkit for loading the ephemeries of the planets. The effect of the Solar Radiation Pressure (SRP) perturbation is included in both the Hill propagator (1) (only cannon-ball model) and the J2000EQ-Ry propagator (2) (flat surface model).

(3) Interfaces between the FD team with the OD, and the AOCS teams require the definition of the *Home Position (HP) reference frame* as shown in Fig. 1. The HP reference frame is used mainly for the mission operation (red dashed rectangle in Fig. 1). The HP reference frame is asteroid-centred. The z_{hp}-axis is along the Earth-Asteroid line, the Sun-Asteroid line belongs to the positive x_{hp}-z_{hp} plane (gray area in Fig. 1) and the y_{hp}-axis is given such that the HP frame is a right-handed coordinate system. Thus:

- The z_{hp}-axis is defined as:

$$\hat{\boldsymbol{r}}_3 = \frac{\boldsymbol{r}_{Earth}}{|\boldsymbol{r}_{Earth}|};$$

- The y_{hp}-axis is defined as:

$$\hat{\boldsymbol{r}}_2 = \frac{\boldsymbol{r}_{Earth} \times \boldsymbol{r}_{Sun}}{|\boldsymbol{r}_{Earth} \times \boldsymbol{r}_{Sun}|};$$

---

[1] In this case, the mean motion is derived from the Ryugu-Asteroid distance at the epoch of deep conjunction (11th December 2018).

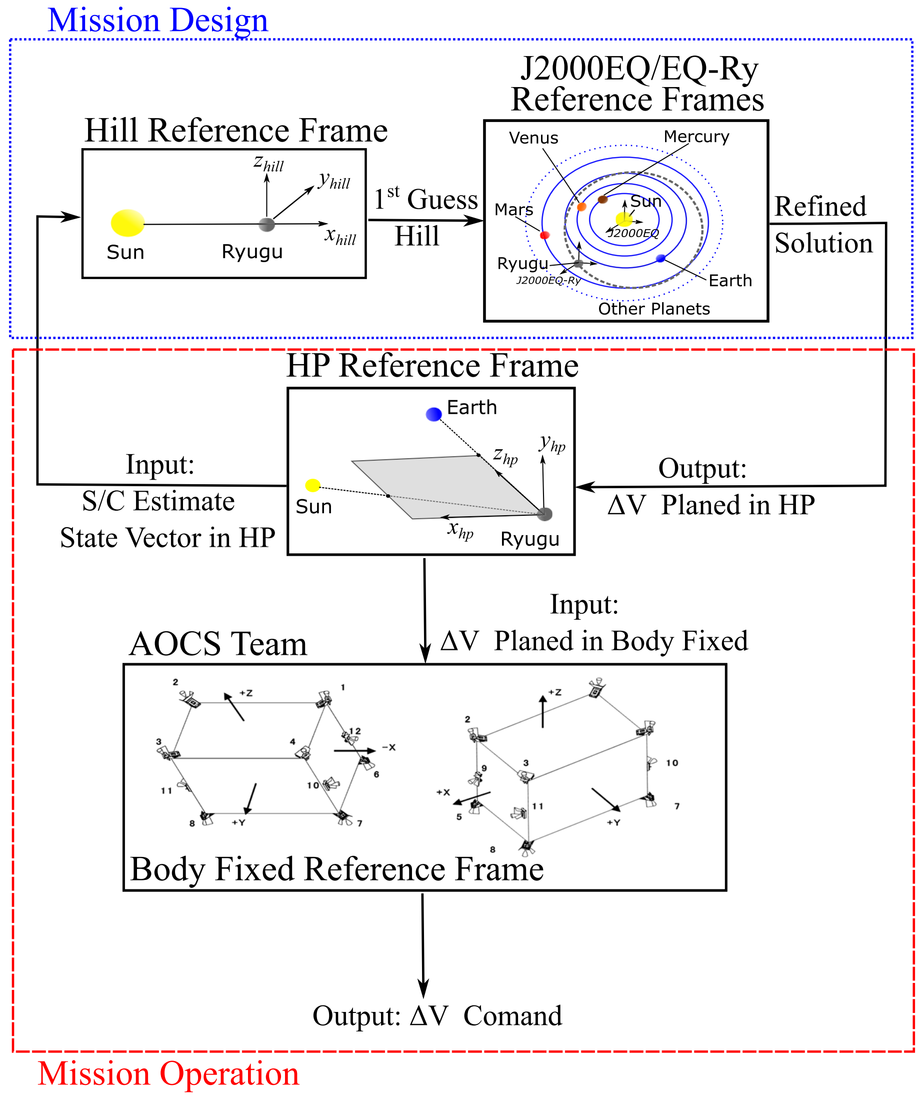

Fig. 1 Schematic overview of the mission design and mission operation for the solar conjunction phase

- The x_{hp}-axis is defined as:

$$\hat{\boldsymbol{r}}_1 = \frac{\left(\frac{\boldsymbol{r}_{Earth}\times\boldsymbol{r}_{Sun}}{|\boldsymbol{r}_{Earth}\times\boldsymbol{r}_{Sun}|}\right)\times\left(\frac{\boldsymbol{r}_{Earth}}{|\boldsymbol{r}_{Earth}|}\right)}{\left|\left(\frac{\boldsymbol{r}_{Earth}\times\boldsymbol{r}_{Sun}}{|\boldsymbol{r}_{Earth}\times\boldsymbol{r}_{Sun}|}\right)\times\left(\frac{\boldsymbol{r}_{Earth}}{|\boldsymbol{r}_{Earth}|}\right)\right|}.$$

Note that $\boldsymbol{r}_{Earth} = \boldsymbol{r}_{Earth|_{J2000EQ}} - \boldsymbol{r}_{Ryugu|_{J2000EQ}}$ and $\boldsymbol{r}_{Sun} = -\boldsymbol{r}_{Ryugu|_{J2000EQ}}$ with

$$\boldsymbol{C}_{HP} = [\hat{\boldsymbol{r}}_1|\hat{\boldsymbol{r}}_2|\hat{\boldsymbol{r}}_3]. \tag{1}$$

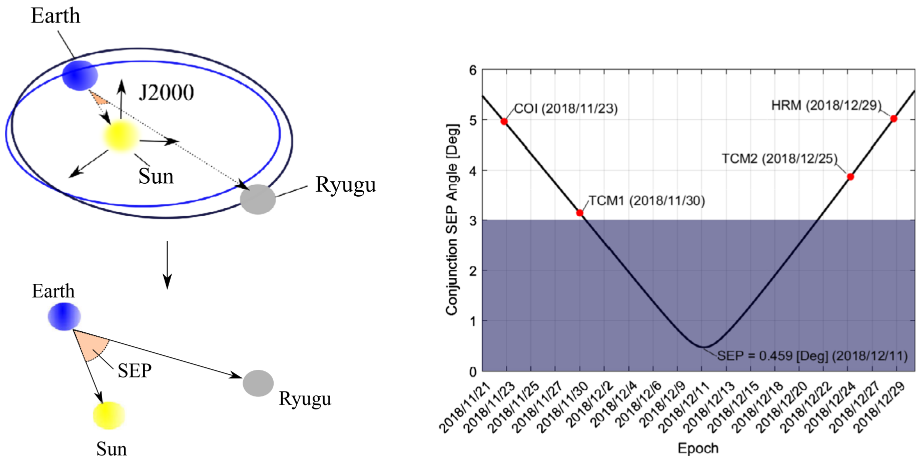

(a) SEP angle. (b) Epoch vs SEP angle.

Fig. 2 The left panel shows the SEP angle definition in the J2000EQ reference frame while the right panel shows the SEP angle as a function of the epoch

This rotational transformation matrix takes coordinates in the HP reference frame (3) to coordinates in the J2000EQ-Ry reference frame (2).

(4) Once the planned ΔV is given in the HP reference frame (3), it has to be transformed in the Hayabusa2 spacecraft's *body fixed reference frame* where the twelve Reaction Control System (RCS)'s thrusters are mounted on the body of the Hayabusa2 spacecraft. This is then send as a ΔV command on board the spacecraft.

This article is devoted to present the activities of the FD team (blue rectangle Fig. 1) while the results of the conjunction mission operation are give in Soldini et al. (2020). The solar conjunction phase is defined by the relative geometry of the Sun, the Earth and the Hayabusa2 Probe. The Sun-Earth-Probe (SEP) angle reaches its minimum value[2] of 0.459° in deep conjunction on the 11th of December 2018 as shown in Fig. 2b. Since the Hayabusa2 spacecraft is usually located at 20 km from Ryugu along the Earth-Ryugu line, the SEP angle can be approximated as the angle between the Earth-Sun line and the Earth-Ryugu line (or Earth-Hayabusa2 probe line) as shown in Fig. 2a.

2.1 Solar Conjunction Mission Operation

The solar conjunction operation is divided in three phases as shown in Table 1. When the SEP angle is $\leq 3°$, the radio communication is disturbed by the solar corona (Morley and Budnik 2007); therefore, it is not safe to send commands to the spacecraft when in deep conjunction (blue area in the right panel of Fig. 2b). In Fig. 2b, the SEP angle is function of the epoch between late November/December 2018. The blue area shows the epochs where the SEP angle is below 3°, when the noise in the Earth-Spacecraft communication signal is affected by the solar corona (Morley and Budnik 2007).

Table 1 highlight the three main phases for the solar conjunction operation: (a) Preparation Phase, (b) Deep Conjunction Phase and (c) Recovery Phase as shown also in Fig. 2b.

---

[2] Note that the Earth and Ryugu orbits are not co-planar; therefore, an exact alignment between Earth-Sun-Ryugu is not reached in this case, so that, in deep conjunction, the SEP angle is not exactly 0°.

Table 1 Solar conjunction mission phases, epochs and SEP angle

Mission phase	Epoch [UTC]	SEP angle [°]
(a) Preparation Phase	2018/11/23-2018/11/30	5-3
(b) Deep Conjunction Phase	2018/12/01-2018/12/21	≤ 3
(c) Recovery Phase	2018/12/22-2018/12/29	3-5

(a) During the preparation phase, the spacecraft performed a 180° slew maneuver around the z_{hp}-axis to ensure the correct orientation of the 12 thrusters after the deep conjunction phase (flip of the HP reference frame). On the 23rd of November 2018, the COI maneuver is performed when the SEP angle is 5° and TCM1 is performed on the 30th of November 2018, when the SEP angle is 3°.

(b) When the spacecraft is in Deep Conjunction (SEP angle $< 3°$), the spacecraft will not perform any orbit maneuver but only attitude maintenance. Beacon operations have been done to monitor the status of the spacecraft while in its highest altitude point of the deep conjunction phase on the 11th of December 2018. The spacecraft stays in deep conjunction for 24 days with no control commands sent from Earth.

(c) The recovery phase requires a second TCM2 maneuver on the 25th of December 2018, when the SEP angle is 4°. The HP Recovery Maneuver (HRM) is performed on the 29th of December 2018 when the SEP angles is 5°.

Four days of observations are planned: two days before deep conjunction and two days right after deep conjunction. As one can see, the two TCMs are scheduled before and after the deep conjunction. However, the two TCMs are not scheduled at the same SEP angle to allow the two days of observation campaign required for the TCM2 maneuver after the deep conjunction phase, Fig. 2b.

3 Equations of Motion in the Hill Problem of the Sun-Ryugu System

The ayu conjunction trajectory is designed in the Hill Reference frame introduced in Sect. 2. We recall that the dynamics of the mother spacecraft are therefore written in a rotating reference frame where the system is centred in the asteroid Ryugu's center of mass. As mentioned in Sect. 2, the Sun and the asteroid are placed along the x_{hill}-axis at a fixed position. The Sun is in the negative x_{hill} coordinates. The photo-gravitation Hill problem is a special approximation of the photo-gravitational Circular Restricted Three Body Problem (CR3BP) where the mass of the secondary body (i.e. asteroid Ryugu) is considered smaller than the mass of the primary body (i.e. the Sun). Therefore, the Hill problem is a subset of the CR3BP where the Sun and the asteroid have fixed relative position along the x_{hill}-axis. When the perturbation of Solar Radiation Pressure (SRP) acceleration is taken into account, the Hill/CR3BP is known as the photo-gravitational Hill/CR3BP. For a Sun-pointing spacecraft, the SRP acceleration has a constant direction as seen from the Hill reference frame. The Hill problem has two equilibrium solutions know as Libration points, L_1 and L_2. When the effect of the SRP acceleration is taken into account, the x_{hill} coordinate of the equilibrium points move towards the Sun and the equilibrium points are here re-named as SL_1 and SL_2 (pseudo Libration points). Depending on how the initial energy of the Spacecraft (state vector) is set, two regions of motion can be distinguished where the spacecraft dynamics are or are not permitted (known as forbidden regions). Those ideas have been used to increase the spacecraft altitude from the nominal operational 20 km (HP position) to a safe spacecraft-asteroid distance grater than 20 km during the conjunction operation. Note that from now on the subscript "$_{hill}$" will be removed when referring to the Hill equations to ease the notation in the paper. Therefore, the Hill equations in dimensional coordinates are given by:

$$\begin{cases} \ddot{x} - 2n\dot{y} = -\frac{\mu_a}{r^3}x + 3n^2x + a_x \\ \ddot{y} + 2n\dot{x} = -\frac{\mu_a}{r^3}y \\ \ddot{z} \qquad\quad = -\frac{\mu_a}{r^3}z - n^2z, \end{cases} \tag{2}$$

where, a_x is the SRP acceleration for a Sun-pointing spacecraft (cannon-ball model) and it is defined as:

$$a_x = a_{x0}\left(\frac{1\ \mathrm{AU}}{d}\right)^2, \tag{3}$$

where a_{x0} is the SRP acceleration at 1 Astronomical Unit (AU):

$$a_{x0} = \frac{P_0}{c}\frac{A}{m}C_r = 1.377 \cdot 10^{-7}\ [\mathrm{m/s^2}]. \tag{4}$$

In Eq. (4), A is the Hayabusa2 spacecraft's reflective area approximated to 13.276 m^2, and its mass, m, of 580 kg. P_0 is the solar flux of 1366 $\mathrm{W/m^2}$, c is the speed of light of $2.99792458 \cdot 10^8$ m/s, and C_r is the reflectivity property of the Hayabusa2 spacecraft assumed as 1.321. The mean anomaly, n, is defined as:

$$n = \sqrt{\frac{\mu_a + \mu_s}{d^3}}. \tag{5}$$

Note that, in our problem, d is the distance of the Sun from the asteroid in the Hill frame at the spacecraft highest altitude location of 1.38 AU (2018/12/11) during the deep conjunction phase. Therefore, the ayu trajectory was designed in the instantaneous Hill reference frame at the 11th of December 2018 epoch rather than considering the average motion of Ryugu around the Sun. This assumption is more appropriate for asteroids with high eccentricity as Ryugu ($e = 0.1902$). The equations of motion of the Hill problem are Hamiltonian and time independent; thus, they admit an energy integral of motion.[3] For a conservative system (i.e. Sun-pointing spacecraft), the energy integral is a constant of motion and it is given by:

$$E = \frac{1}{2}\left(\dot{x}^2 + \dot{y}^2 + \dot{z}^2\right) - \frac{\mu_a}{r} - \frac{3}{2}n^2x^2 + \frac{1}{2}n^2z^2 - a_x x. \tag{6}$$

For the conjunction epoch at 1.38 AU (2018/12/11), a_x was computed as $7.1442 \cdot 10^{-11}\ \mathrm{km\,s^{-2}}$. The equations of equilibrium can be found by setting the velocities and the accelerations of Eq. (2) equal to zero, and in particular we get:

$$-\frac{\mu_a}{r^3}x + 3n^2x + a_x = 0. \tag{7}$$

For a_x equal to zero (non reflective case) the coordinate of the libration point is simply $x_{L_{2,1}} = \pm\sqrt[3]{\frac{\mu_a}{3n^2}}$ which is ±89.62 km (radius of the Hill sphere, in Fig. 3a). For a Sun-pointing spacecraft with reflectivity coefficient equal to the Hayabusa2 case ($C_r = 1.321$), the 3rd order equation in Eq. (7) was solved which gives the coordinates of the pseudo libration points as $x_{\mathrm{SL}_2} = 21.03$ km and $x_{\mathrm{SL}_2} = -1{,}606.78$ km (Fig. 3b).

---

[3] Note that in celestial mechanics "$-2E$" is often used which is called the Jacobi integral either known with the symbol C or J.

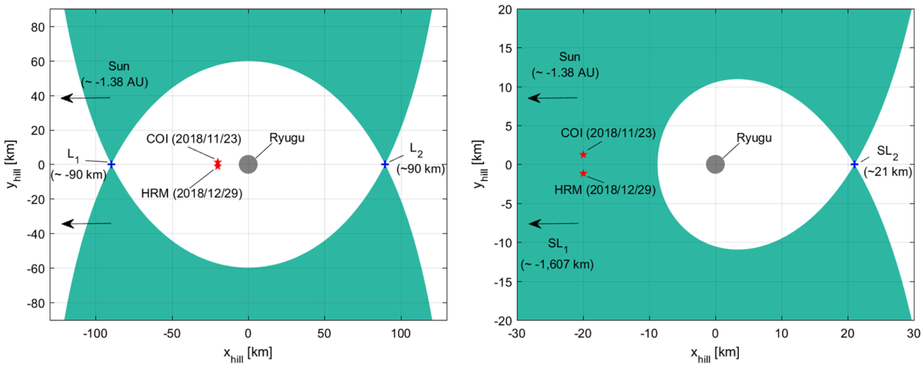

(a) $C_r = 0$ (b) $C_r = 1.321$

Fig. 3 The left panel shows the dynamical objects (ZVC and equilibrium points) when the effect of SRP is neglected, while the right panel shows the same dynamical object for the Hayabusa2 spacecraft. In both cases, the dynamical objects are computed for the instantaneous Hill problem in deep conjunction (2018/12/11)

The green areas in Fig. 3 are regions where the spacecraft motion is not permitted. Conversely, the white area in Fig. 3 represents the region of possible motion for the spacecraft. Therefore, if the energy of the spacecraft is below the energy of either $L_{1,2}$ (for $C_r = 0$) or SL_2 (for $C_r = 1.321$), the spacecraft motion can be naturally bounded and constrained around Ryugu. The boundary line between the white and the green areas is called the Zero Velocity Curve (ZVC). As the name suggests, points that lie on the ZVC line have zero velocities. To obtain the ZVC in Fig. 3, the velocities in Eq. (6) are set to zero. Therefore, the critical energy is defined as:

$$E^* = -\frac{\mu_a}{r} - \frac{3}{2} n^2 x^2 + \frac{1}{2} n^2 z^2 - a_x x. \tag{8}$$

The ZVC can be found by setting the z-coordinate to zero in Eq. (8) while x and y are free to vary. The intersection of the potential surface E^* with a fixed energy constant results in the ZVC appearance in the x-y plane. The ZVC and its forbidden regions disappear if the energy is above the energy level of SL_1 (E_{SL_1}) and the spacecraft motion is permitted for any x-y coordinates. In Fig. 3, the Home Position (HP) point at COI and HRM is ($C_r = 0$, Fig. 3a) or isn't ($C_r = 1.321$, Fig. 3a) inside the Hill sphere depending on the spacecraft's reflectively property. Therefore, the energy of the Hayabusa2 spacecraft at HP point must be above the SL_2 energy. This means that due to the reflectively of the Hayabusa2 spacecraft, its motion is not bounded around Ryugu and ΔV maintenance for station-keeping at the HP location must be given every 1-2 days.

Using this notion and adapting it to the superior solar conjunction phase, we make use of the energy integral, E, to confine the Hayabusa2 spacecraft motion along a low energy transfer trajectory (ayu-shape) with a consequent low fuel expenditure.

4 Low Energy Ayu Conjunction Trajectory Design for Hovering Spacecraft

The ayu conjunction trajectory has a fixed Time of Flight (ToF) and it depends on the selected SEP (Sun-Earth-Probe) angle. The SEP angle is function of the epoch and it was introduced in Fig. 2 (Sect. 2). The epoch associated to the minimum SEP angle is the reference

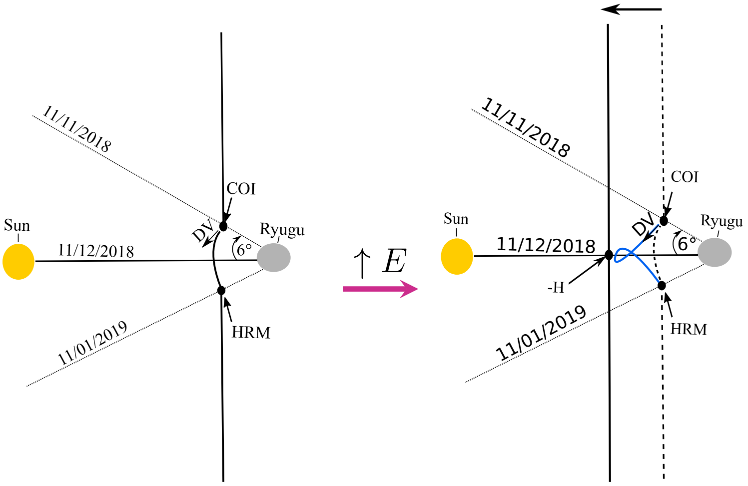

(a) Before the COI maneuver. (b) After the COI maneuver.

Fig. 4 A cartoon representation of the chosen instantaneous Hill problem at the 2018/12/11 epoch (highest altitude in deep conjunction, $-H$) for the design of the conjunction trajectory. The HP position at COI and HRM are represented in the epoch of the maneuver that for 6° in the SEP angle corresponds to 2018/11/11 at COI and to 2019/01/11 at HRM respectively

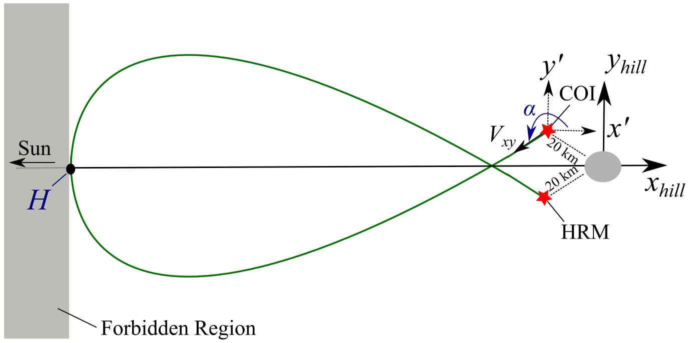

Fig. 5 A cartoon representation of the trajectory conjunction design: optNEAR's shooting method

frozen epoch used for the design of the conjunction trajectory as shown in Fig. 4. Figure 4 shows a schematic idea behind the proposed conjunction trajectory. Figure 4a shows the ZVC before the ΔV is given at COI, while Fig. 4b shows how the effect of the maneuver moves the ZVC towards the Sun at an altitude of $-H$ in the x-coordinates of the Hill reference frame. As shown in Fig. 4-5, the major design constraint of the conjunction trajectory requires the spacecraft to depart from HP before deep conjunction (COI's red star in Fig. 5) and to return to HP after deep conjunction (HRM's red star in Fig. 5). It is well know that a trajectory approaching the ZVC or the forbidden regions inverts naturally its motion.

Our main idea was to look for a trajectory that can encounter the forbidden region at an altitude with x-coordinate, $-H$, greater than -20 km (HP). H is an unknown variable of our problem and it is shown in both Fig. 4 and Fig. 5. Once the SEP angle has been fixed, the position at COI and HRM epochs are also fixed as shown in Fig. 4 for 6° in the SEP angle. Note that the velocity of the spacecraft is artificially kept equal to zero at the HP point (COI or HRM). The HP position keeping is known as Hayabusa2's BOX-A operation that was already introduced in Sect. 2. Knowing that the COI and HRM positions are fixed and lie almost in the x-y plane of the Hill reference frame, the conjunction trajectory was expected to be planar with insertion velocity at COI (v_z close to zero). This holds true if the spacecraft is kept at HP point in nominal condition of zero velocity. As a first approximation, a symmetric conjunction trajectory with respect to the x-z plane was expected. The insertion velocity at COI is related to the unknown parameter H. We made use of the ZVC notion to lead our thinking towards the design of the shooting method proposed here.

The altitude $-H$ is chosen to belong to the ZVC, therefore $-H$ is a point of zero velocity by definition as shown in Fig. 4-5. This relates the velocity of the spacecraft directly with the coordinate $-H$ through Eq. (6). However, Eq. (6) gives information of the modulus of the velocity and not of its components. To solve the two boundary problem between COI and HRM (red stars in Fig. 5), we introduce the angle α and a local reference frame centered at COI (x', y', z') as shown in Fig. 5. For navigation purposes, the Hayabusa2 spacecraft has to be on the day side of the asteroid, therefore the planar COI injection velocity, V_{xy} has to be in the II or III quadrant of the x', y' coordinates frame ($90° < \alpha < 270°$). However, due to the geometry of the problem, we can limit α further by knowing that at $-H$ the velocity of the spacecraft will be inverted. Therefore to reach HRM V_{xy} has to be in the III quadrant ($180° < \alpha < 270°$) if the SEP angles are between 4°-6°. The geometry of the conjunction trajectory can be intuitively understood by imagining the game of pool where a ball strikes a rail and bounces off it (here the "rail" is the ZVC of the forbidden regions).

The main parameters used for designing the trajectory are H, α and v_z as shown in blue in Fig. 5. Note that V_{xy} is function of v_z. Once the Time of Flight (ToF) (or SEP) and μ_a are selected, the trajectory has to satisfy a two boundary value problem where the position at the insertion velocity (COI) and the position at braking velocity (HRM) are fixed. The optimum trajectory can be found as a function of H (the maximum trajectory distance from the center of the Hill reference frame), α (the in plane direction of the insertion velocity) and v_z (the z component of the insertion velocity in the Hill reference frame). v_z is kept as an optimal parameter as the trajectory is not perfectly symmetric along the x-z plane.

To find the nominal conjunction trajectory, the main steps of the proposed single shooting method (optNEAR tool) are as follow:

1) From Eq. (6), the energy associated to the altitude $-H$ is given as:

$$E_H = -\frac{\mu_a}{H} - \frac{3}{2}n^2H^2 - a_xH, \tag{9}$$

where the energy, E_H, is associated to a point that belongs to the ZVC therefore the state vector is $\{-H, 0, 0, 0, 0, 0\}$.

2) Once the altitude of the forbidden region is set (read the energy E_H), we can find the modulus of the insertion velocity at COI as followed by re-organizing Eq. (6):

$$V = \sqrt{2E_H + 2\frac{\mu_a}{r_0} + 3n^2x_0^2 - n^2z_0^2 + 2a_xx_0}, \tag{10}$$

note that the initial position of COI in the Hill reference frame is given by $\{x_0, y_0, z_0\}$. This position can be found by knowing the initial state at COI in the previously introduced HP reference frame {0 km, 0 km, 20 km} in Sect. 2 and by applying the transformation from the HP reference frame to the Hill reference frame. The details are given in Appendix A.

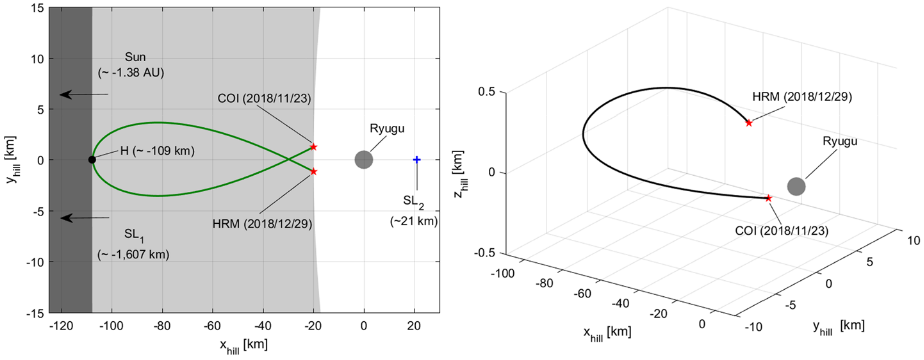

Fig. 6 Nominal ayu conjunction trajectory as designed in the Hill frame. The left panel shows two forbidden regions: before (light gray area) and after (dark gray area) the COI maneuver. Note that the HP position lies on the ZVC of the light gray forbidden region; while the $-H$ coordinate lies on the ZVC of the dark gray region. The right panel shows a 3D view of the conjunction trajectory

3) The first guess of the COI insertion velocity is given by:

$$\boldsymbol{v}_0 = \begin{Bmatrix} V_{xy} \cos \alpha_0 \\ V_{xy} \sin \alpha_0 \\ v_{z_0} \end{Bmatrix}, \tag{11}$$

with $V_{xy} = \sqrt{V^2 - v_{z0}^2}$ and V being the module of $\boldsymbol{v}_0$ obtained from Eq. (10).

4) The initial guess in point 3) is used to solve Eq. (2) through ODE integration. The time of integration corresponds to the selected ToF by assuming the following initial state vector:

$$\boldsymbol{X}_0 = \begin{Bmatrix} x_0 \\ y_0 \\ z_0 \\ V_{xy} \cos \alpha_0 \\ V_{xy} \sin \alpha_0 \\ v_{z_0} \end{Bmatrix} \tag{12}$$

5) After the integration at Step 4), we can find the final state, $\boldsymbol{X}_f$, and compare the expected final position ($\boldsymbol{r}_{HRM}$) with the one computed at the end of the ODE integration ($\boldsymbol{r}_f$). We can thus find H, α and v_z that minimize the following cost function:

$$\min_{H,\alpha,v_z} ||\boldsymbol{r}_{HRM} - \boldsymbol{r}_f||. \tag{13}$$

The boundary conditions are given as $180^\circ < \alpha < 270^\circ$, $-0.001 < v_z < 0.001$ km/s and $80 < H < 800$ km. As a first guess, $H_0 = 300$ km, $\alpha_0 = 188^\circ$ and $v_{z_0} = 0$ km/s were assumed. Figure 6 shows the designed conjunction trajectory for the nominal case ($\mu_a = 32\ \mathrm{m}^3\,\mathrm{s}^{-2}$ and the SEP angle equal to 5°). The presented shooting algorithm was developed in the optNEAR tool. The 3D view of the nominal conjunction trajectory is shown in the right panel of Fig. 6. As one can see, the conjunction trajectory is not perfectly planar because the HP z-coordinate at COI (-168 m in z) and HRM (361.7 m in z) epochs do not lie on the x-y plane. The left panel in Fig. 6 shows the forbidden regions. The conjunction trajectory has a "fish-like" shape that we named as "ayu" (sweetfish in Japanese) trajectory.

Table 2 Designed trajectory for different SEP angles (or ToFs) and μ_a with $\frac{A}{m}Cr$ equal to 0.0302 $\frac{\text{m}^2}{\text{kg}}$

Epoch	SEP [°]	μ_a [m^3/s^2]	ToF [day]	$\bar{H}$ [km]	$\bar{\alpha}$ [°]	$\bar{v_z}$ [mm/s]
2018/11/26 - 2018/12/26	4	11	29.98	80.00	186.32	0.1615
2018/11/23 - 2018/12/29	5	11	35.97	104.44	187.45	0.1552
2018/11/18 - 2018/01/02	6	11	44.97	148.57	189.17	0.1471
2018/11/26 - 2018/12/26	4	32	29.98	83.53	186.04	0.1434
2018/11/23 - 2018/12/29	5	32	35.97	107.79	187.18	0.1275
2018/11/18 - 2018/01/02	6	32	44.97	151.46	188.91	0.1075
2018/11/26 - 2018/12/26	4	92	29.98	91.60	185.55	0.0998
2018/11/23 - 2018/12/29	5	92	35.97	115.68	186.66	0.0585
2018/11/18 - 2018/01/02	6	92	44.97	158.69	188.36	0.0056

The light gray area represents the energy of the Hayabusa2 spacecraft in the Hill reference frame when in hovering position (Home Position), while the dark gray is the case of the energy of the spacecraft once the insertion velocity is given at COI (energy increase). The expected maximum distance from Ryugu is of 109 km (2018/12/11) for the nominal case. Table 2 shows the optimum parameters for the design of the ayu conjunction trajectory as a function of the Ryugu's gravity constant, μ_a, and the SEP angles (or ToFs). As one can see, larger SEP angles correspond to longer ToF and consequently higher altitude, H, can be reached. Moreover, for a fixed SEP angle, higher μ_a results in higher H reached. Therefore, uncertainties in the Ryugu's gravity parameter mean that the spacecraft might be closer or farther from the center of the asteroid.

For the conservation of the kinetic and potential energy, the theoretical expected ΔV cost in the hill reference frame to increase and decrease the altitude of the spacecraft from 20 km to 109 km and finally back to 20 km can be computed as:

$$\Delta V_{hill} = 2\sqrt{2a_x \Delta h} = 2\sqrt{2a_x(109\text{ km} - 20\text{ km})} = 0.2255\text{ m/s} \tag{14}$$

The total ΔV computed with the optNEAR tool's shooting method is of 0.2359 m/s which is consistent with the theoretical expected value. Table 3 shows the energy integral for: the libration points, the H coordinate and the HP position at COI or HRM, where $E_{\text{SL}_2} < E_{COI/HRM} < E_H < E_{\text{SL}_1}$.

Figure 7 shows a cartoon of the conjunction trajectory where the spacecrafts attitude is assumed to be kept constant and pointing in the x negative coordinate. The ayu trajectory is almost symmetrical along the x-z axis by keeping the velocities in x and z equal to zero at $-H$ and this configuration allows to keep the asteroid in the FoV of the wide angle camera, ONC-W1 (60°). Therefore, the ayu conjunction trajectory demonstrates to respect all the required constraints at low fuel costs and it has been selected as a reference solution for the Hayabusa2's solar conjunction phase.

5 Robustness to Uncertainties in the Deterministic Maneuvers

The ayu conjunction trajectory meets the major operation constraints. In this section, the robustness of the deterministic maneuvers and the required guidance maneuvers (stochastic ΔVs) are investigated as function of the maneuver uncertainties.

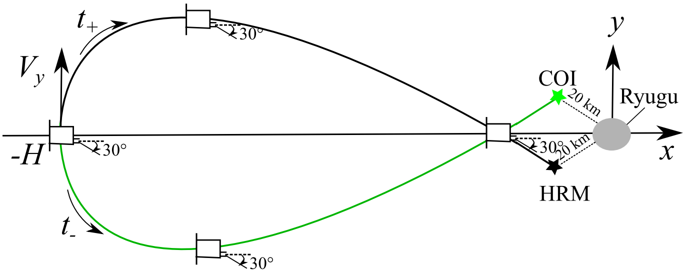

Fig. 7 A cartoon of the conjunction trajectory and the ONC-W1 camera's FOV

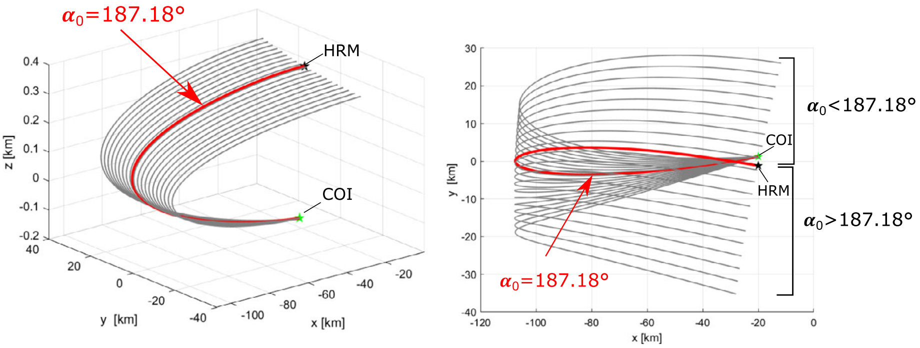

(a) 3D view.

(b) 2D view.

Fig. 8 Reference solution for 5° in the SEP angle and μ_a equal 32 m^3/s^2 (red). Solutions for α equal to 187.18° ± 5° (gray)

Table 3 Energy integral for the libration points, the coordinate H and the HP points (COI/HRM)

Point	x_{hill} [km]	E [$\frac{m^2}{s^2}$]	$\frac{A}{m}Cr$ [$\frac{m^2}{kg}$]
$L_{2,1}$	±89.62	−5.355881189297829e-04	0
SL_1	−1607.00	5.738617055213259e-02	0.0302
SL_2	21.00	−3.033890971893174e-03	0.0302
H	−109.00	7.145604567030928e-03	0.0302
COI/HRM (HP)	−20.00	−1.828397609511783e-04	0.0302

5.1 Uncertainty in the COI Maneuver

Figure 8 shows the effect of the uncertainties in the COI maneuver in the planar (x-y) case where an error in the planar velocity, V_{xy}, orientation angle, α presented in the in Sect. 4 of the optNEAR tool's shooting method was considered. The reference ayu trajectory for a SEP angle of 5° and μ_a of 32 m^3/s^2 presented in Table 2 was selected and it is marked in red in Fig. 8. As shown in Table 2, the optimum α is for 187.18°. An uncertainty of ±5° in α has been considered and the resulting trajectories are shown in gray in Fig. 8. The modules of the in-plane velocity V_{xy} and out-of plane velocity v_{z_0} were kept constant. Figure 8b shows that for $\alpha < 187.18°$, the spacecraft will be in the positive y-coordinates at the HRM epoch while it will be in the negative y-coordinates for $\alpha > 187.18°$.

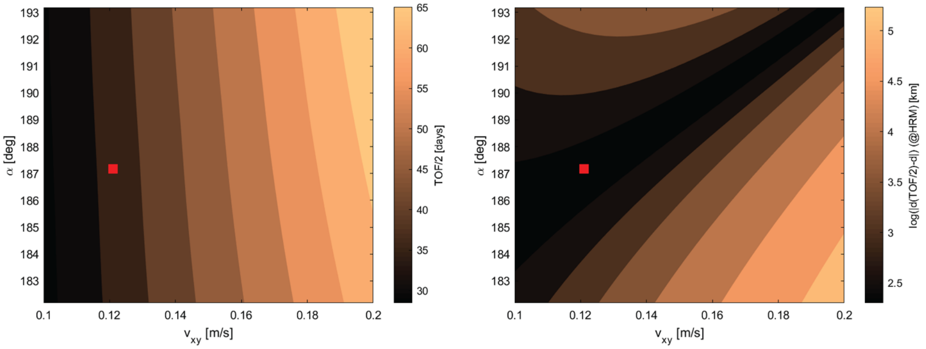

(a) ToF/2.

(b) Position error at HRM in log scale.

Fig. 9 Half of the ToF and position error at HRM as function of $182.18° < \alpha < 193.18°$ and the module of the in-plane velocity $0.1 < V_{xy} < 0.2$ m/s

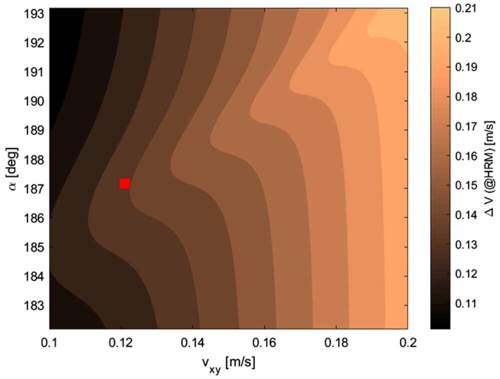

Fig. 10 ΔV maneuver at HRM as a function of uncertainties in the COI maneuver for $182.18° < \alpha < 193.18°$ and the module of the in-plane velocity $0.1 < V_{xy} < 0.2$ m/s

Figure 9 shows the effect of the uncertainties in α and on the in-plane velocity at COI on to the ToF (Fig. 9a) of the ayu trajectory and the final error at the HRM point (Fig. 9b). The red square represents the nominal solution. The ToF increases with the increase of V_{xy} and it has little dependency on α as shown in Fig. 9a. This can be understood by looking at the energy equation, Eq. (6) where a higher module in the velocity increases the energy of the spacecraft and it can be expected that the altitude H will be farther away from the center of the asteroid. This holds also true for lower module in the velocity at COI where it can be expected a shorter ToF to reach HRM position. The highest error in the HRM position is found for high V_{xy} (i.e. 0.2 m/s) and lower α ($< 187.18°$) as shown in Fig. 9b. This can be explained by Fig. 8b where solutions with $\alpha < 187.18°$ bring the spacecraft to the positive y-coordinates while HRM is positioned in the negative y-coordinates resulting in position errors of 250 km (5.5 km in log scale) for the worst case scenario

Figure 10 shows the effect of the COI maneuver uncertainties on the ΔV at HRM. The solution is function of the uncertainties in $182.18° < \alpha < 193.18°$ and in the module of the in-plane velocity $0.1 < V_{xy} < 0.2$ m/s. The red square in Fig. 10 highlights the solution for the nominal ayu trajectory of Table 2.

The module of the ΔV at HRM is primarily influenced by the in-plane velocity V_{xy} and its dependency with α shows that for a given V_{xy} there exist a optimum α angle that minimizes the ΔV at HRM. It is possible to notice that the effect of uncertainties in α and

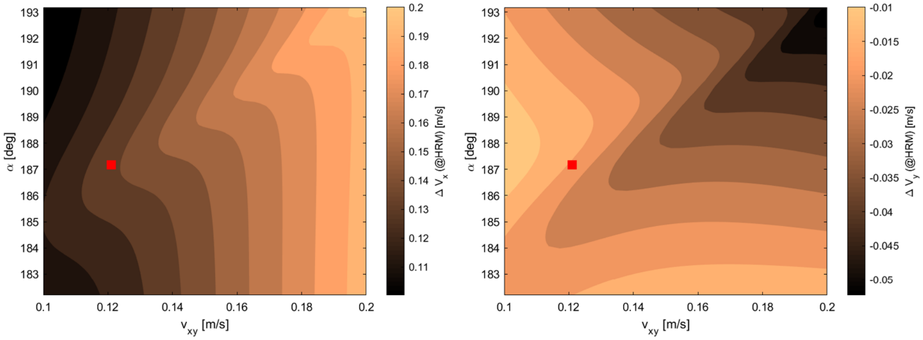

(a) $\Delta \mathrm{V}_x$ at HRM in m/s. (b) $\Delta \mathrm{V}_y$ at HRM in m/s.

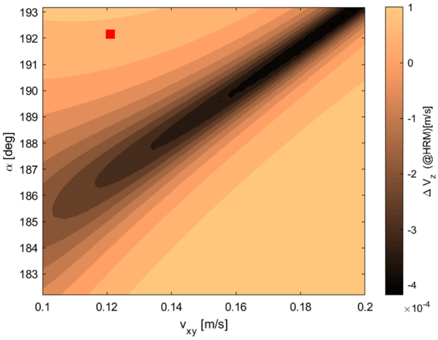

(c) $\Delta \mathrm{V}_z$ at HRM in m/s.

Fig. 11 ΔV maneuver at HRM as a function of uncertainties in the COI maneuver for $182.18° < \alpha < 193.18°$ and the module of the in-plane velocity $0.1 < V_{xy} < 0.2$ m/s: x, y, z components

Fig. 12 A cartoon of the conjunction trajectory and HRM maneuver

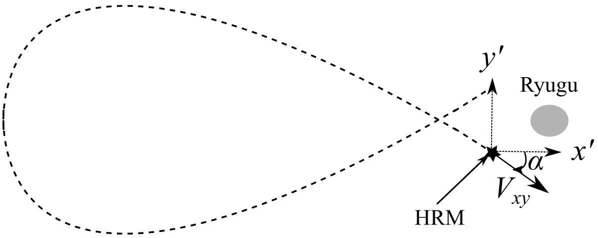

in V_{xy} results in higher ΔV at HRM in the x direction as shown in Fig. 11. From Fig. 11, it is possible to conclude that α and V_{xy} do not affect much the y and z components of the ΔV at HRM.

5.2 Uncertainty in the HRM Maneuver

This section investigates the effect of uncertainties in the HRM maneuver at the end of the conjunction phase. Figure 12 shows a schematic representation of the ayu conjunction trajectory at its final arrival at the HRM point (20 km altitude from Ryugu on the 29th of November 2018). Two parameters of uncertainties were considered, the in-plane velocity

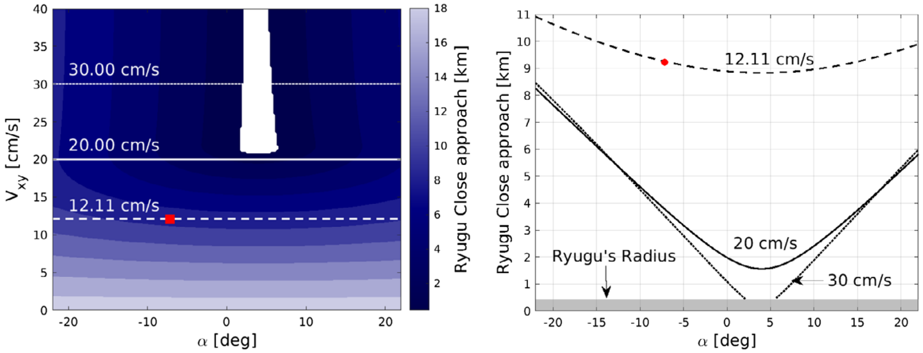

(a) CA Map. (b) CA vs α (white lines Fig. 13a).

Fig. 13 Close Approach (CA) distance from Ryugu as function of uncertainties in α and in the in-plane velocity V_{xy}. The red square highlights the solution for the nominal ayu trajectory. Three cases are highlighted for V_{xy}: (1) 12.11 cm/s (nominal ayu trajectory, dashed line), (2) 20 cm/s (solid line) and (3) 30 cm/s (dot lines)

V_{xy} and its orientation angle, α. Figure 13a shows the map of the Close Approach (CA) distance from Ryugu in km after 1 day of integration time from the HRM location as function of $-22^\circ < \alpha < 22^\circ$ and the in-plane velocity $0 < V_{xy} < 40$ cm/s. This is the contingency scenario in which we considered the robustness of the ayu conjunction trajectory against failures in executing the HRM maneuver at the HRM point allowing a 1 day margin for rescheduling the HRM maneuver.

In Fig. 13, three solutions for V_{xy} are highlighted in white in Fig. 13a and in black in Fig. 13b. The nominal ayu trajectory case with V_{xy} equal to 12.11 cm/s in dashed line, the case of 20 cm/s in solid line and the case of 30 cm/s in dot lines.

For uncertainties in V_{xy} less than 20 cm/s, the spacecraft will not impact on Ryugu after 1 day of simulation starting from the HRM position. Conversely, for $V_{xy} > 20$ cm/s, the spacecraft can potentially impact on Ryugu when $0^\circ < \alpha < 9^\circ$ (white area of Fig. 13a). Moreover, arrival velocities, V_{xy}, at HRM below 18 cm/s are not of much concern if the HRM maneuver is missed because the CA distance has little dependency from α. Therefore, the solution of the nominal ayu trajectory for $V_{xy} = 12$ cm/s (white dashed line in Fig. 13a) allows recovery maneuvers for any uncertainties in α. The red square marks the nominal ayu trajectory for $\alpha = -7.2^\circ$ and $V_{xy} = 12.11$ cm/s at HRM.

Figure 13b shows the dependency of CA for a fixed V_{xy} in this case 12.11 cm/s which correspond to the white dashed line solution in the CA map of Fig. 13a). As one can see, the spacecraft maintains a distance from Ryugu between 9-11 km allowing to reschedule a recovery maneuver to reach the desired 20 km altitude in the BOX-A operation.

5.3 Contingency Study: Recovery Trajectory

A contingency study is here carried out to demonstrate the robustness of the selected ayu conjunction trajectory. Figure 14 shows a schematic representation of the possible contingency scenario. Following the result of Sect. 5.2, this case scenario study a possible recovery trajectory when the ΔV maneuver at HRM on 29th of December 2018 is cancelled. The proposed strategy assumes that a recovery ΔV will be given a day after the HRM position on the 30th of December 2018. The recovery position is of $\{-1.97, 0.41, 9\}$ km in the HP reference frame and it was obtained by numerical forward integration from the HRM position. This final position is quite far from the desired HP position of $\{0, 0, 20\}$ km in the HP co-

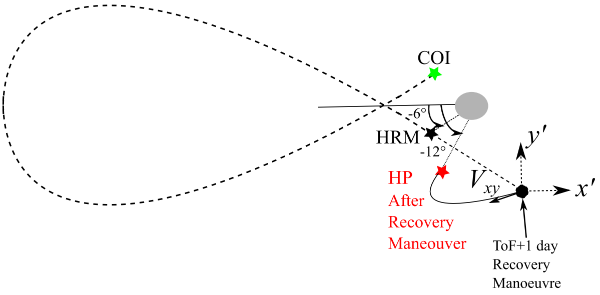

Fig. 14 Schematic representation of a possible recovery trajectory for the case of missed opportunity to execute the HRM manoeuvre (black star). The red star represent the final recovery point

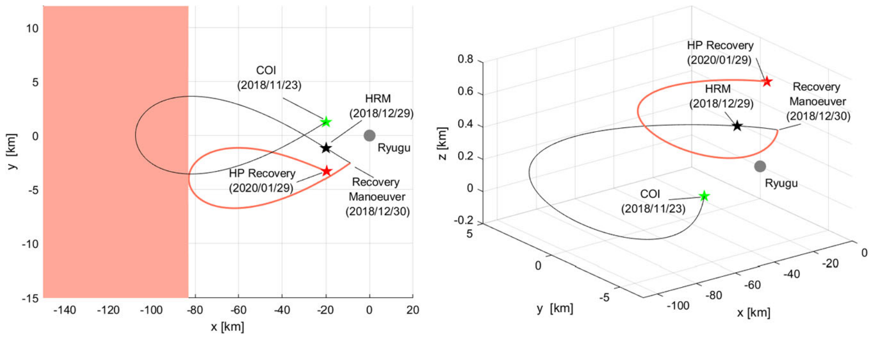

(a) Forbidden region (red area) of the Recovery Trajectory (red line).

(b) 3D view of the planned ayu (black) and recovery trajectories (red).

Fig. 15 Recovery operation: the black trajectory is the designed ayu trajectory between COI (green star) and HRM (black start). The recovery maneuver is executed 1 day after the HRM point. The red star is the HP position after 1 month from the recovery position

ordinates after the conjunction. Figure 15 shows the optimum recovery trajectory from the 30th of December 2018 until the 29th of January 2019 (20 km altitude from Ryugu). The optNEAR's shooting method presented in Sect. 4 was modified in point 3) where the recovery trajectory starts from the recovery location rather than at COI and the epochs have been changed accordingly. However, the core idea of the presented method holds true for the recovery case.

Figure 15a shows the forbidden region (red area) associated to the recovery trajectory (red line). The energy of the recovery trajectory (forbidden region's red area in Fig. 15a) is lower than the energy of the ayu trajectory (forbidden region's dark gray area in Fig. 6). Finally, Fig. 15b shows the ayu and the recovery trajectories as seen in the Hill reference frame. The boundary conditions for the recovery trajectory are: $188° < \alpha < 195°$, $-0.001 < v_z < 0.001$, and $40 < H < 90$ km. The initial guess in the optimum parameters were set as: $H_0 = 70$ km, $\alpha = 190°$ and $v_{z_0} = 0$ km/s. The optimum parameters after the optimisation method are given by: $\bar{\alpha} = 188.36°$, $\bar{H} = 83.17$ km and $\bar{v_z} = 0.81$ mm/s.

6 Robustness to Uncertainties in the Navigation at Home Position (HP-NAV)

Once the robustness of the ayu trajectory has been verified against uncertainties in the deterministic maneuvers (at COI and HRM), we are now interested to verify the effect of the navigation uncertainties at HP position on the COI maneuver.

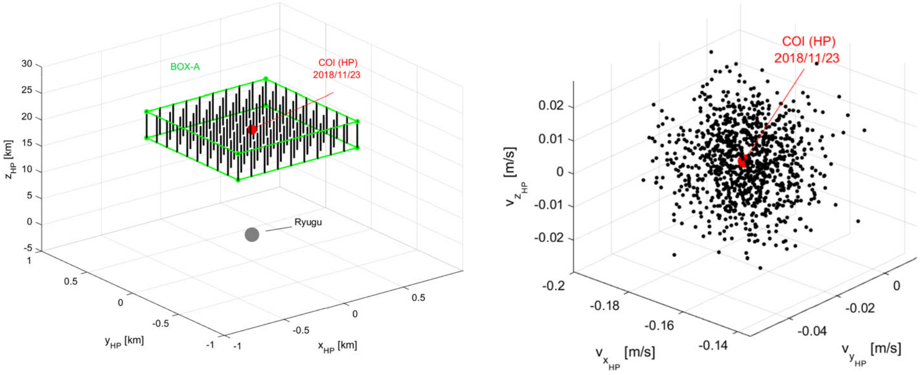

(a) BOX-A positions (black dots).

(b) 3σ distribution in velocity.

Fig. 16 Uncertainties in the HP maintenance NAVigation (HP-NAV) within BOX-A (in green). Possible distribution in position and velocities at COI

For any Hayabusa2 proximity operations, the spacecraft is kept within the nominal operation box named A (BOX-A). BOX-A is centered at the HP altitude around 20 km in the HP reference frame introduced in Sect. 2. When the spacecraft is in BOX-A, the navigation requires a ΔV maneuver every 1/2 days to keep the spacecraft inside the BOX-A (know as HP-NAV or HP maintenance). Therefore, the COI operation has to account for the effects of the navigation in BOX-A. For the uncertainty analysis, we considered a uniform distribution in the position uncertainties (Fig. 16a). The spacecraft can be potentially located anywhere within the BOX-A. A Gaussian distribution was selected for the uncertainty in the COI's insertion velocity (Fig. 16b). The nominal COI position is shown in red in Fig. 16. The following parameters have been considered:

- Uniform distribution in position within the BOX-A:
  - $x_{HP} = y_{HP} = \pm 0.5$ km
  - $z_{HP} = 20 \pm 2.5$ km
- Gaussian distribution in velocity in the HP reference frame: $3\sigma = [0.5,\ 0.7,\ 1]$ cm/s, for example see Fig. 16b

We kept the same assumptions for the SEP angle and μ_a as shown in Table 2. Note that the coordinates are given in the HP reference frame and they have to be expressed in the Hill reference frame through the transformation given in Appendix A. The uncertainty analysis is carried out in the Hill problem. We aim to verify if correction maneuvers (stochastic ΔVs) between COI and HRM are required.

6.1 Uncertainty in HP-NAV Position

For the HP-NAV uncertainty in position, a uniform distribution of 3000 points within the BOX-A (green box in Fig. 16) was considered. The velocity at COI was kept to its nominal value. Figure 17 shows the final position at HRM in the Hill reference frame, starting from initial states at COI as shown in Fig. 16a. In Figs. 18, Ryugu gravity's is set to 32 $\mathrm{m}^3/\mathrm{s}^2$. In Fig. 18, figures that belong to the same column as Fig. 18.a, Fig. 18.d and Fig. 18.g show the results for increasing values in the SEP angles from 4° to 6°. Rows of figures in Fig. 18 show the same SEP angle solution but with different views for example for a SEP angle of

Fig. 17 Uncertainty manifold for $\mu_a = 32\ \mathrm{m}^3/\mathrm{s}^2$ and $\mathrm{SEP} = 5°$

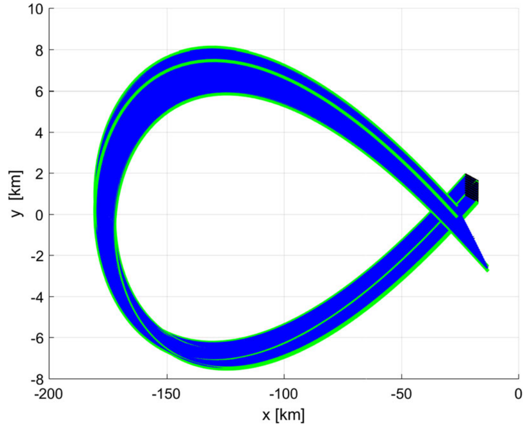

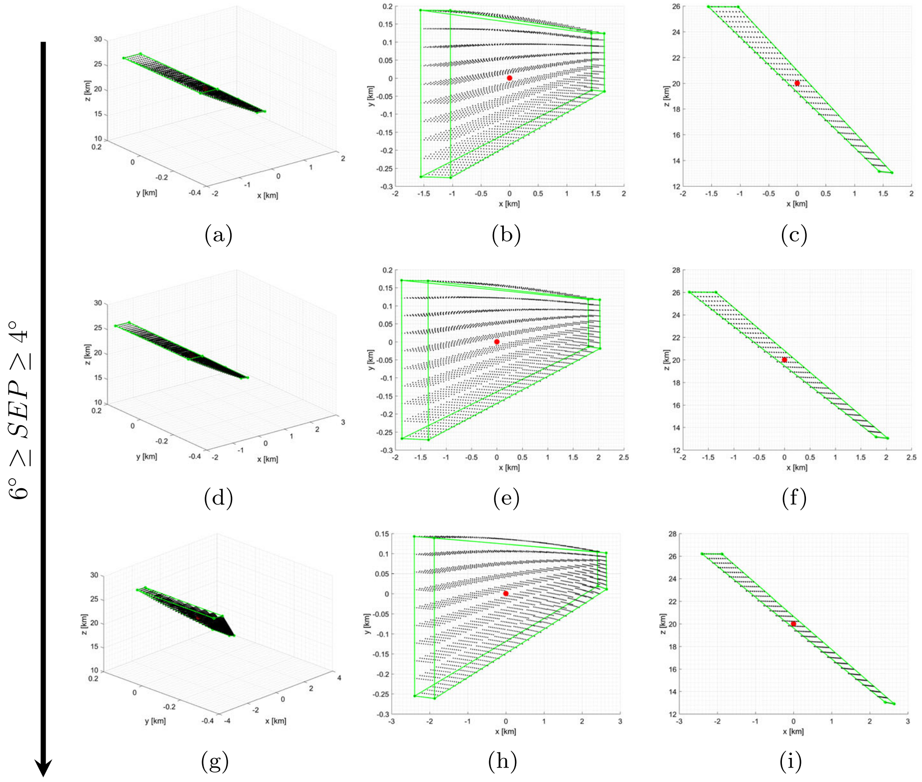

Fig. 18 Dispersion in position at HRM: $\mu_a = 32\ \mathrm{m}^3/\mathrm{s}^2$

5° it shows a 3D view (Fig. 18.a), a planar view in the x-y plane (Fig. 18.b) and a planar view in the x-z plane (Fig. 31.c). As one can notice, if the spacecraft is initially inside the BOX-A at COI, it will be inside the final box at HRM. This suggests that the conjunction trajectory is robust in error in the HP-NAV position. The same analysis was carried out for Ryugu's gravity equal to 11 $\mathrm{m}^3/\mathrm{s}^2$ (nominal case shown in Fig. 31, Appendix B) and

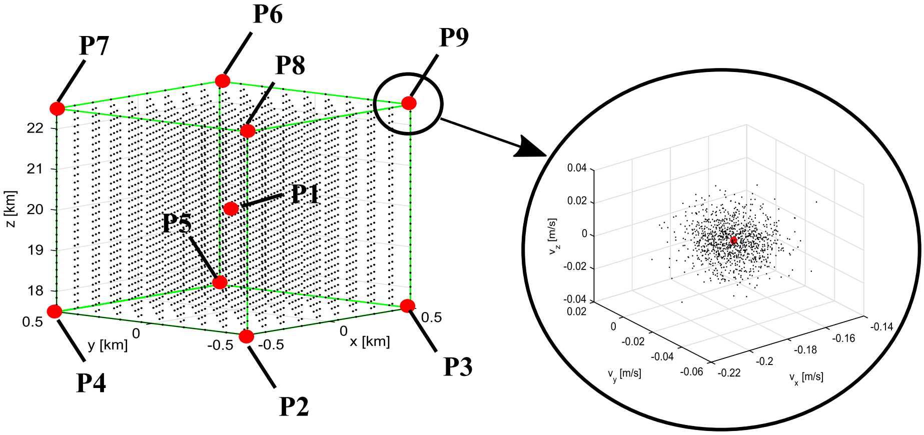

Fig. 19 Gaussian distribution of the HP-NAV velocity uncertainty (1000 solutions). Nine positions (P1-P9) were selected

92 m^3/s^2 (Fig. 32, Appendix B). From this analysis, we concluded that the corners of the BOX-A are the only representative cases to perform the uncertainty analysis in velocity.

Therefore, instead of using the full set of 3000 solutions, only 9 points (the 8 corners of BOX-A and the nominal solution, HP position at COI) will be considered. Figure 17 shows a 3D view of the manifold (blue trajectories) associate to BOX-A when Ryugu's gravity is 32 m^3/s^2. Further solutions can be found in Appendix B for $\mu_a = 11$ and 92 m^3/s^2.

6.2 Uncertainty in HP-NAV Velocity

In this section, the effect of velocity uncertainty in the HP-NAV at COI are investigated. The nominal case of $3\sigma = 5$ mm/s is presented here (for the other solutions refer to Appendix C). Figure 19 shows the number of solutions analysed. For each of the nine solutions (P1-P9) (red dots), a 3σ Gaussian distribution of 1000 solutions were analysed such that in Fig. 20-21 9000 solutions are computed at the end of the simulation. As before, rows of figures in Fig. 20-21 shows how the solution evolves for increasing gravity coefficient (left to right), μ_a, while columns of figures show the dependency for increasing SEP angle (top to bottom).

Figure 20 shows the Gaussian distribution in position at HRM for $3\sigma = 5$ mm/s of uncertainty at COI while Fig. 21 shows the distribution of the arrival velocity at HRM. Tables 4 and 5 show the 1σ error in both the final position (Fig. 20) and velocity (Fig. 21) at HRM for all the six cases. The maximum errors are in the Hill x-coordinate for solution c in Fig. 20-21 with a 3σ error of 44.4 km in position and 17.25 cm/s.

Based on this results and the one in Appendix C we concluded that at least one stochastic maneuver (TCM) right after the deep conjunction phase is required. We also concluded that error in the execution ΔVs during the mission operation below or equal 4 mm/s can be accepted. Therefore, error in the main ΔVs above 4 mm/s will require a contingency correction ΔV (trim ΔVs).

7 Design of the Trajectory Correction Maneuver (TCM)

The Trajectory Correction Manoeuvre (TCM) is designed by solving a two boundary value problem where the initial position at TCM and the final position at HRM are fixed. From the

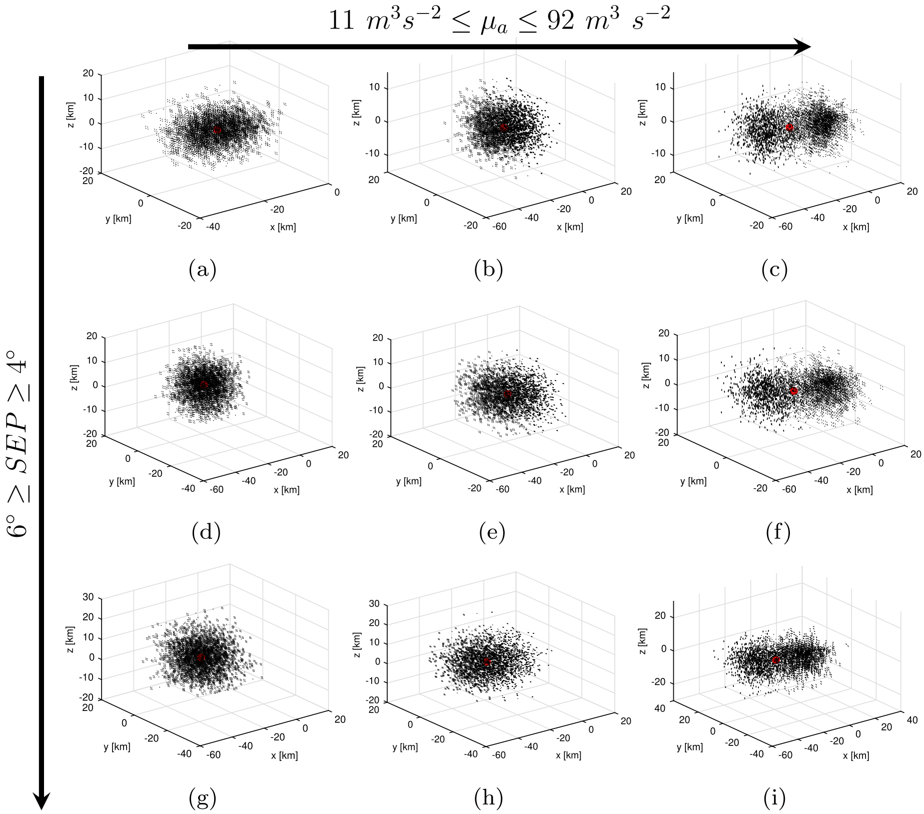

Fig. 20 Final position at HRM with HP-NAV velocity distribution of $3\sigma = 5$ mm/s at COI

Table 4 Reference position at HRM ± 1σ with $3\sigma = 5$ mm/s at COI

SEP [°]	μ_a [m^3/s^2]					
	11		32		92	
4	a)	$x = -19.97 \pm 5.97$ km $y = -0.960 \pm 4.45$ km $z = 0.320 \pm 4.15$ km	b)	$x = -19.97 \pm 7.80$ km $y = -0.960 \pm 4.26$ km $z = 0.320 \pm 3.87$ km	c)	$x = -19.97 \pm 14.80$ km $y = -0.960 \pm 4.300$ km $z = 0.320 \pm 3.670$ km
5	d)	$x = -19.96 \pm 6.86$ km $y = -1.160 \pm 5.25$ km $z = 0.362 \pm 5.00$ km	e)	$x = -19.96 \pm 8.55$ km $y = -1.160 \pm 5.10$ km $z = 0.362 \pm 4.96$ km	f)	$x = -19.96 \pm 14.69$ km $y = -1.160 \pm 5.460$ km $z = 0.362 \pm 4.433$ km
6	g)	$x = -19.94 \pm 8.41$ km $y = -1.437 \pm 6.46$ km $z = 0.415 \pm 6.30$ km	h)	$x = -19.94 \pm 9.81$ km $y = -1.437 \pm 6.46$ km $z = 0.415 \pm 5.97$ km	i)	$x = -19.94 \pm 15.36$ km $y = -1.437 \pm 7.140$ km $z = 0.415 \pm 5.620$ km

previous analysis, we concluded that at least one TCM is required after deep conjunction (SEP ∼ 0°). Once the spacecraft reaches its highest altitude along the ayu trajectory, a TCM is scheduled at SEP = 4° as shown in Fig. 22. The ToF is fixed and is the time frame between

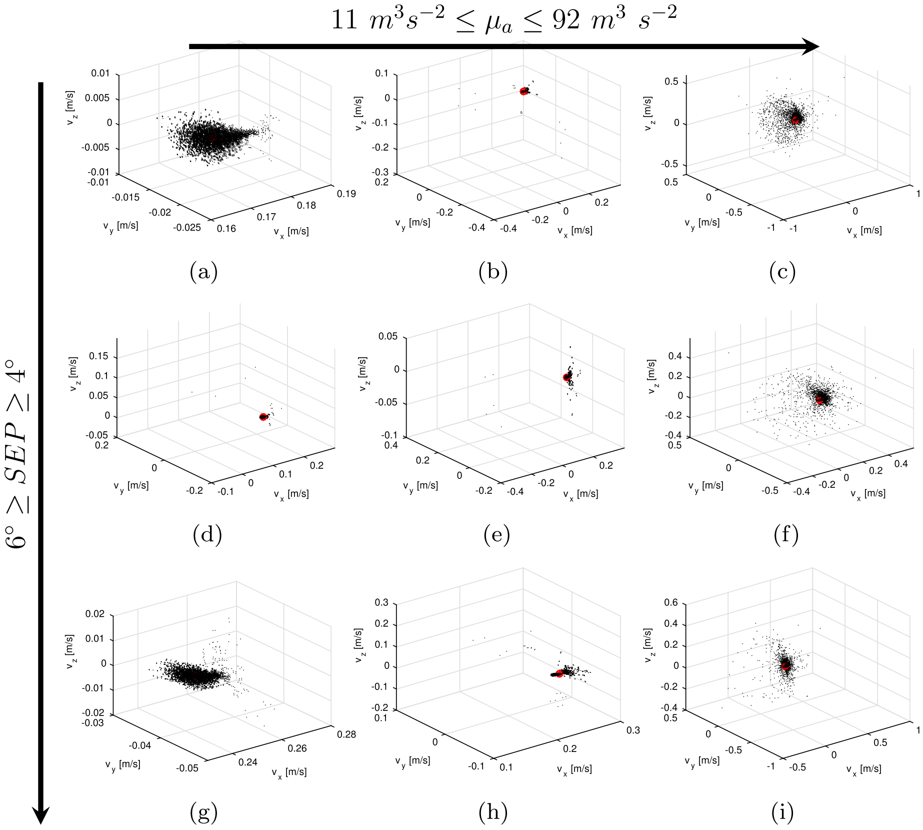

Fig. 21 Final velocity at HRM with HP-NAV velocity distribution of $3\sigma = 5$ mm/s at COI

Table 5 Reference velocity at HRM $\pm\ 1\sigma$ with $3\sigma = 5$ mm/s at COI

SEP [°]	μ_a [m^3/s^2]		
	11	32	92
4	a) $v_x = 17.03 \pm 0.31$ cm/s $v_y = -1.854 \pm 0.14$ cm/s $v_z = 0.014 \pm 0.12$ cm/s	b) $v_x = 17.66 \pm 1.15$ cm/s $v_y = -1.889 \pm 0.48$ cm/s $v_z = 0.009 \pm 0.46$ cm/s	c) $v_x = 19.34 \pm 5.74$ cm/s $v_y = -1.985 \pm 5.12$ cm/s $v_z = -0.003 \pm 4.57$ cm/s
5	d) $v_x = 20.10 \pm 0.46$ cm/s $v_y = -2.600 \pm 0.26$ cm/s $v_z = 0.014 \pm 0.27$ cm/s	e) $v_x = 20.64 \pm 1.05$ cm/s $v_y = -2.634 \pm 0.59$ cm/s $v_z = 0.010 \pm 0.29$ cm/s	f) $v_x = 22.11 \pm 3.71$ cm/s $v_y = -2.725 \pm 3.95$ cm/s $v_z = -0.002 \pm 3.51$ cm/s
6	g) $v_x = 24.52 \pm 0.33$ cm/s $v_y = -3.937 \pm 0.16$ cm/s $v_z = 0.014 \pm 0.13$ cm/s	h) $v_x = 24.96 \pm 0.66$ cm/s $v_y = -3.968 \pm 0.42$ cm/s $v_z = 0.010 \pm 0.70$ cm/s	i) $v_x = 26.18 \pm 3.04$ cm/s $v_y = -4.055 \pm 3.02$ cm/s $v_z = -0.002 \pm 3.04$ cm/s

the TCM epoch and the ToF at HRM. Therefore, a ODE integration that uses Eq. (2) is done and the error between the final desired position and the expected position is computed. Finally, the insertion velocity at TCM is found through the minimisation of the following

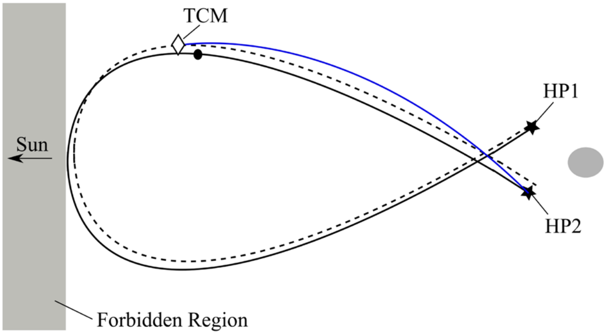

Fig. 22 Shooting method for the TCM manoeuvre design

cost function:

$$\min_{V_x,V_y,V_z} ||\boldsymbol{r}_{HRM} - \boldsymbol{r}_f||. \tag{15}$$

Note that the ΔV at TCM is the difference between the TCM insertion velocity and the velocity of the spacecraft before the TCM manoeuvre. We adopted a conservative approach so that a second TCM maneuver is scheduled before the spacecraft enters in deep conjunction. As part of the guidance in the conjunction phase, we have to compute two TCMs (stochastic ΔVs) as mentioned in Sect. 2.

8 Preliminary Guidance and Navigation Design: Consider Parameters Covariance Analysis

A complete and exact knowledge of the spacecraft state vector is generally not possible. The individual state variables cannot be measured precisely and available measurements are usually function of the state variables. The spacecraft motion can be affected by non-modelled forces which are not adequately represented in the dynamical model. Its model parameters can be uncertain too. By definition, the linearized system of equations of the nonlinear dynamics is a further approximation. These sources of error make the knowledge of the spacecraft's state uncertain. The computation of the most likely current state of the spacecraft in the presence of measurements and model uncertainty is the focus of orbit determination which will not be studied in this paper. The error analysis instead involves an investigation of the impact of various sources of error on the orbit determination. The output of an error analysis, as done in this paper, provides the magnitudes of the state vector variances and covariances, thus quantifying the relative contribution of the significant error sources for a preliminary guidance and navigation design (Gordon 1991).

In the first part of this article, the design of the ayu conjunction trajectory has been presented. The second part of this article is devoted to investigate the preliminary OD error analysis for this newly proposed trajectory. The technique used here involves the linearisation of the nonlinear equations of motion around a reference solution (nominal ayu path) and then applying linear estimation techniques (Tapley et al. 2004). The OD process is thus changed from estimating the state of the linear, time-varying, deviations from the reference trajectory. The reference solution used here is generated by numerical integration of a high-fidelity nonlinear equations of motion in the optNEAR tool. As OD is out of the scope of this analysis, the current work focuses only on the consider parameters covariance analysis that includes the uncertainties in the dynamical model and in the measurements (Montenbruck

Table 6 Standard Deviation in the HP coordinates at COI

3σ	Optimistic	Pessimistic
$3\sigma_{X_{HP}}$ [m]	180	670
$3\sigma_{Y_{HP}}$ [m]	180	440
$3\sigma_{Z_{HP}}$ [m]	100	1400
$3\sigma_{VX_{HP}}$ [mm/s]	2	7
$3\sigma_{VY_{HP}}$ [mm/s]	2	4
$3\sigma_{VZ_{HP}}$ [mm/s]	0.5	16

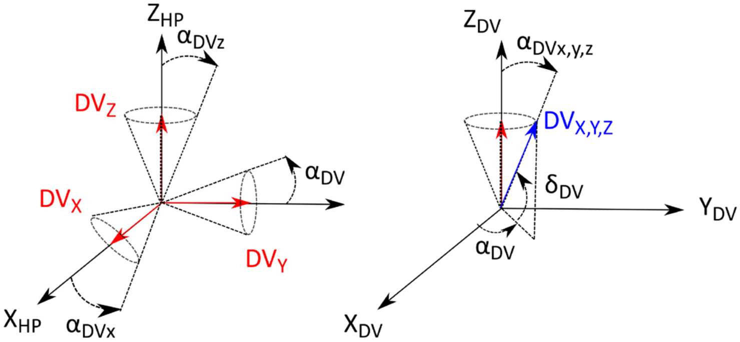

(a) HP Frame. (b) ΔV Frame.

Fig. 23 Uncertainties in the ΔV maneuver module and direction in the ΔV reference frame

and Gill 2005; Tapley et al. 2004; Gordon 1991). The scope of the covariance analysis is to compute the covariance matrix after some tracking and to estimate the stochastic ΔVs at TCMs.

In this article, the linear covariance analysis is carried out to account for uncertainties in the HP-NAV (initial knowledge error) at the COI maneuver (20 km from the asteroid), the GCP-NAV or OpNav (two-way Doppler and ONC-T or ONC-W1 cameras) and ΔV-maneuver execution error. The covariance analysis is carried out considering three trajectory legs: from COI to TCM1 (Leg 1), from TCM1 to TCM2 (Leg 2) and from TCM2 to HRM (Leg 3). The uncertainties in the navigation are considered independently for only Leg 1 and Leg 2. The epochs of the maneouvers for the reference conjunction trajectory are shown in Table 1.

8.1 Initial Knowledge at COI

Before the insertion ΔV is given at COI, the HP-NAV navigation error was taken into account through the initial knowledge covariance matrix, $\boldsymbol{P}_{0,\,hp}$, given in the HP coordinates as shown in Table 6.

8.2 ΔV-Maneuver Execution Error

Figure 23a shows the three independent $\boldsymbol{\Delta V}_{HP}$ along the X_{HP}, Y_{HP} and Z_{HP} coordinate of the HP reference frame. In Fig. 23b, a local reference frame aligned with the ΔV direction is considered (Wagner and Goodson 2008). This $\boldsymbol{\Delta V}_{HP}$ is given by transforming the

Table 7 Uncertainties in the manoeuvre execution

Item	3σ	Units
ΔV_{x-hp}	15% nominal	[km/s]
ΔV_{y-hp}	15% nominal	[km/s]
ΔV_{z-hp}	$5 \cdot 10^{-6}$	[km/s]
$\alpha_{\Delta V_{x-hp}}$	2.5	[°]
$\alpha_{\Delta V_{y-hp}}$	2.5	[°]
$\alpha_{\Delta V_{z-hp}}$	2.5	[°]

nominal $\boldsymbol{\Delta V}_{J2000EQ}$ from the J2000EQ reference frame to the HP reference frame. The ΔV execution error uncertainties are given in the module and in the pointing direction. Three independent covariance matrices for the X_{HP}, Y_{HP}, Z_{HP} components were considered. The assumption made in the pointing accuracy and in the velocity module are shown in Table 7. The process noise covariance matrix is given by:

$$\boldsymbol{P}_{n,\ hp} = \begin{bmatrix} \mathbf{0}_{3\times3} & \mathbf{0}_{3\times3} \\ \mathbf{0}_{3\times3} & \boldsymbol{P}^{(3\times3)}_{ExErr,\ hp} \end{bmatrix} \tag{16}$$

where $\boldsymbol{P}^{(3\times3)}_{ExErr,\ hp}$ is derived from the assumption made in Fig. 23.

8.3 Navigation Error: Consider Parameters Covariance Matrix

The consider parameters covariance analysis is a batch weighted least square formulation that also includes parameters uncertainty. For an unbiased system with a sufficient number of observations, the covariance matrix will asymptotically approach zero and the estimation algorithm will be insensitive to any further observations. This condition can lead to filter divergence. A possible approach to prevent this divergence is to recognize that the linearised equations are in error. To compensate for this error, we assumed that the error in the linearised equations is due to uncertain parameters called considered parameters. They are a priori estimates and the associated covariance matrix is known. Therefore, the nonlinear dynamical model in J2000EQ coordinates is given by (Tapley et al. 2004):

$$\begin{cases} \dot{\boldsymbol{X}} &= \boldsymbol{F}(\boldsymbol{X}, \boldsymbol{C}, t) \\ \dot{\boldsymbol{Y}}_i &= \boldsymbol{G}(\boldsymbol{X}_i, \boldsymbol{C}, t_i) + \boldsymbol{\epsilon}_i \end{cases} \tag{17}$$

The first equation in the system of Eq. (17) is a compact form of the N-Body dynamics written in J2000EQ-Ry coordinates, for further details in the propagator developed in optNAER tool refer to Appendix D. $\boldsymbol{C}$ is the vector of the considered parameters. Note that the vector $\boldsymbol{C}$ can be divided in the dynamical model considered parameters, $\boldsymbol{C_d}$, and measurements model parameters, $\boldsymbol{C_m}$:

$$\boldsymbol{C} = \begin{bmatrix} \boldsymbol{C_d} \\ \boldsymbol{C_m} \end{bmatrix} \tag{18}$$

By expanding Eq. (17) in a first order Taylor series around the nominal ayu trajectory, Eq. (17) turns into:

$$\begin{cases} \dot{\boldsymbol{x}}(t) = \boldsymbol{A}(t)\boldsymbol{x}(t) + \boldsymbol{B}(t)\boldsymbol{c}(t) \\ \boldsymbol{y}_i \quad = \tilde{\boldsymbol{H}}_i \boldsymbol{x}_i + \tilde{\boldsymbol{H}}_{ci} \boldsymbol{c} + \boldsymbol{\epsilon}_i \end{cases} \tag{19}$$

where $\boldsymbol{c}(t) = \boldsymbol{C}(t) - \boldsymbol{C}_*(t)$ is the residual of the consider parameters. $\boldsymbol{C}$ is the nominal vector of the consider parameters and $\boldsymbol{C}_*$ is the reference vector.

$$\boldsymbol{A} = \left[\frac{\partial \boldsymbol{F}}{\partial \boldsymbol{X}}\right]_* \qquad \boldsymbol{B} = \left[\frac{\partial \boldsymbol{F}}{\partial \boldsymbol{C}}\right]_* = \left[\begin{matrix} \frac{\partial \boldsymbol{F}}{\partial \boldsymbol{C}_d} & \frac{\partial \boldsymbol{F}}{\partial \boldsymbol{C}_m} \end{matrix}\right]_* \tag{20}$$

The matrix $\boldsymbol{A}$ is the matrix of the linearised equations. Note that $\left[\frac{\partial \boldsymbol{F}}{\partial \boldsymbol{C}_m}\right]_* = \boldsymbol{0}$ as the measurements model parameters do not appear in the dynamical model. In order to compute the observation at a time t_i different from the observation epoch, the state transition matrix has to be computed. The state transition matrices associated to the state and the consider parameters are numerically computed through:

$$\begin{cases} \dot{\boldsymbol{\Phi}}(t, t_0) = \boldsymbol{A}(t)\boldsymbol{\Phi}(t, t_0) \\ \dot{\boldsymbol{\Theta}}(t, t_0) = \boldsymbol{A}(t)\boldsymbol{\Theta}(t, t_0) + \boldsymbol{B}(t) \end{cases} \tag{21}$$

with $\boldsymbol{\Theta}(t_0, t_0) = \boldsymbol{0}$ and $\boldsymbol{\Phi}(t_0, t_0) = \boldsymbol{I}$. Note that:

$$\boldsymbol{\Theta}(t, t_0) = \frac{\partial \boldsymbol{X}(t)}{\partial \boldsymbol{C}(t_0)} = \left[\begin{matrix} \frac{\partial \boldsymbol{X}(t)}{\partial \boldsymbol{C}_d(t_0)} & \frac{\partial \boldsymbol{X}(t)}{\partial \boldsymbol{C}_m(t_0)} \end{matrix}\right] \tag{22}$$

with $\frac{\partial \boldsymbol{X}(t)}{\partial \boldsymbol{C}_m(t_0)} = \boldsymbol{0}$. The sensitivity matrix for both the state vector and the consider parameters are defined as:

$$\tilde{\boldsymbol{H}}_i = \left[\frac{\partial \boldsymbol{F}_i}{\partial \boldsymbol{C}_i}\right]_* \qquad \tilde{\boldsymbol{H}}_{ci} = \left[\frac{\partial \boldsymbol{G}_i}{\partial \boldsymbol{C}_i}\right]_* \tag{23}$$

We make use of the state transition matrices to compute the observations at time t_i so that:

$$\boldsymbol{y}_i = \tilde{\boldsymbol{H}}_i \left[\boldsymbol{\Phi}(t_i, t_0)\boldsymbol{x}_0 + \boldsymbol{\Theta}(t_i, t_0), \boldsymbol{c}\right] + \tilde{\boldsymbol{H}}_{ci}\boldsymbol{c} + \boldsymbol{\epsilon}_i \tag{24}$$

The sensitivity matrix are finally computed as

$$\boldsymbol{H}_i = \tilde{\boldsymbol{H}}_i \boldsymbol{\Phi}(t_i, t_0) \qquad \boldsymbol{H}_{ci} = \tilde{\boldsymbol{H}}_i \boldsymbol{\Theta}(t_i, t_0) + \tilde{\boldsymbol{H}}_{ci} \tag{25}$$

The consider parameters filter is given by solving the following set of equations:

$$\begin{cases} \dot{\boldsymbol{x}}(t) = \boldsymbol{A}(t)\boldsymbol{x}(t) + \boldsymbol{B}(t)\boldsymbol{c}(t) \\ \boldsymbol{y}_i \quad = \boldsymbol{H}_i\boldsymbol{x}_0 + \boldsymbol{H}_{ci}\boldsymbol{c} + \boldsymbol{\epsilon}_i \end{cases} \tag{26}$$

8.4 Observations and the Sensitivity Matrix ($\bar{\boldsymbol{H}}$)

In our analysis, the measurements in the range and the range rate are assumed to be along the Earth-Spacecraft line. The azimuth and elevation angles are measured from the spacecraft (Gordon 1991) ($-\boldsymbol{r}$) as shown in Fig. 24. The observations vector, $\boldsymbol{y}$, is defined as:

$$\boldsymbol{y} = \begin{Bmatrix} \rho \\ \dot{\rho} \\ \alpha \\ \delta \end{Bmatrix} = \begin{Bmatrix} \sqrt{(x - x_e)^2 + (y - y_e)^2 + (z - z_e)^2} \\ \frac{(x-x_e)(vx-vx_e)+(y-y_e)(vy-vy_e)+(z-z_e)(vz-vz_e)}{\sqrt{(x-x_e)^2+(y-y_e)^2+(z-z_e)^2}} \\ \tan^{-1}\left(\frac{y}{x}\right) \\ \sin^{-1}\left(-\frac{z}{r}\right) \end{Bmatrix}, \tag{27}$$

Table 8 Measurements for the Leg 1: From COI to TCM1

Observation	Date and time	Step [sec]	1σ
2-way Doppler	2018/11/28 00:00-06:00	60	5 [mm/s]
2-way Doppler	2018/11/29 00:00-06:00	60	5 [mm/s]
2-way Range	2018/11/28 01:00-02:00	60	10 [m]
2-way Range	2018/11/29 01:00-02:00	60	10 [m]
ONC-W1/T Case 1	2018/11/27 06:00 - 2018/11/29 02:00	1024	60°/1024 (-W1) or 6°/1024 (-T)
ONC-W1/T Case 2	2018/11/26 06:00 - 2018/11/29 02:00	1024	60°/1024 (-W1) or 6°/1024 (-T)
ONC-W1/T Case 3	2018/11/25 06:00 - 2018/11/29 02:00	1024	60°/1024 (-W1) or 6°/1024 (-T)

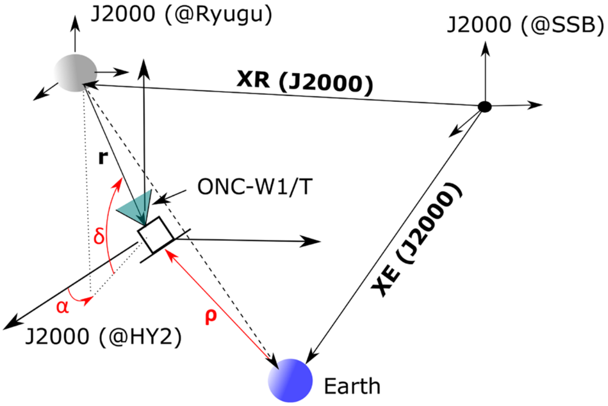

Fig. 24 Reference frames and measurements (in red)

with $r = \sqrt{x^2 + y^2 + z^2}$ (spacecraft-asteroid distance). x_e, y_e and z_e are the coordinates of the Earth[4] as seen from Ryugu in the J2000EQ reference frame. We can now compute the sensitivity matrix following the definition given in Eq. (23):

$$\tilde{\boldsymbol{H}} = \begin{bmatrix} \frac{x-x_e}{\rho} & \frac{y-y_e}{\rho} & \frac{z-z_e}{\rho} & 0 & 0 & 0 \\ \frac{(vx-vx_e)}{\rho} - \frac{(\boldsymbol{\rho}\cdot\dot{\boldsymbol{\rho}})(x-x_e)}{\rho^3} & \frac{(vy-vy_e)}{\rho} - \frac{(\boldsymbol{\rho}\cdot\dot{\boldsymbol{\rho}})(y-y_e)}{\rho^3} & \frac{(vz-vz_e)}{\rho} - \frac{(\boldsymbol{\rho}\cdot\dot{\boldsymbol{\rho}})(z-z_e)}{\rho^3} & \frac{(x-x_e)}{\rho} & \frac{(y-y_e)}{\rho} & \frac{(z-z_e)}{\rho} \\ -\frac{y}{x^2+y^2} & \frac{x}{x^2+y^2} & 0 & 0 & 0 & 0 \\ \frac{zx}{r^3\sqrt{1-(\frac{z}{r})^2}} & \frac{zy}{r^3\sqrt{1-(\frac{z}{r})^2}} & \frac{1}{r^2\sqrt{1-(\frac{z}{r})^2}}\left[\frac{z^2}{r} - r\right] & 0 & 0 & 0 \end{bmatrix}. \tag{28}$$

$\tilde{\boldsymbol{H}}$ is the measurement matrix and it is a time-varying matrix function of Eq. (27). The expected measurements are given in Table 8 and Table 9 for Leg 1 and Leg 2 respectively where we assumed a 2-days observation campaign before each TCM. The assumed Gaussian distribution (1σ) is given in the list below:

- 1σ Range Rate [km/s]: 5e-06
- 1σ Range [km]: 0.01
- 1σ Azimuth = Elevation (ONC-W1) [rad]: 0.00102265
- 1σ Azimuth = Elevation (ONC-T) [rad]: 0.000102265

---

[4] This is often the tracking station rather than the Earth position.

Table 9 Measurements for the Leg 2: From TCM1 to TCM2

Observation	Date and time	Step [sec]	1σ
2-way Doppler	2018/12/23 00:00-06:00	60	5 [mm/s]
2-way Doppler	2018/12/24 00:00-06:00	60	5 [mm/s]
2-way Range	2018/12/23 01:00-02:00	60	10 [m]
2-way Range	2018/12/24 01:00-02:00	60	10 [m]
ONC-W1/T Case 1	2018/12/22 06:00 - 2018/12/24 02:00	1024	60°/1024 (-W1) or 6°/1024 (-T)
ONC-W1/T Case 2	2018/12/21 06:00 - 2018/12/24 02:00	1024	60°/1024 (-W1) or 6°/1024 (-T)
ONC-W1/T Case 3	2018/12/20 06:00 - 2018/12/24 02:00	1024	60°/1024 (-W1) or 6°/1024 (-T)

8.5 Consider Parameter Covariance Matrix ($\boldsymbol{B}$)

We have chosen the spacecraft reflectively coefficient, Cr, and the camera accuracy, $\Delta\alpha$ and $\Delta\delta$ as consider parameters. Their standard deviations are given as follow:

- 1σ Azimuth = Elevation (ONC-W1) [rad]: 0.00102265 (as before)
- 1σ Azimuth = Elevation (ONC-T) [rad]: 0.000102265 (as before)
- 3σ Cr: 10%

The consider parameters matrix $\boldsymbol{B}$ is derived through (Montenbruck and Gill 2005; Tapley et al. 2004):

$$\boldsymbol{B} = \begin{bmatrix} \frac{\partial F_1}{\partial Cr} & \frac{\partial F_1}{\partial \Delta\alpha} & \frac{\partial F_1}{\partial \Delta\delta} \\ \frac{\partial F_2}{\partial Cr} & \frac{\partial F_2}{\partial \Delta\alpha} & \frac{\partial F_2}{\partial \Delta\delta} \\ \frac{\partial F_3}{\partial Cr} & \frac{\partial F_3}{\partial \Delta\alpha} & \frac{\partial F_3}{\partial \Delta\delta} \\ \frac{\partial F_4}{\partial Cr} & \frac{\partial F_4}{\partial \Delta\alpha} & \frac{\partial F_4}{\partial \Delta\delta} \\ \frac{\partial F_5}{\partial Cr} & \frac{\partial F_5}{\partial \Delta\alpha} & \frac{\partial F_5}{\partial \Delta\delta} \\ \frac{\partial F_6}{\partial Cr} & \frac{\partial F_6}{\partial \Delta\alpha} & \frac{\partial F_6}{\partial \Delta\delta} \end{bmatrix} = \left[\boldsymbol{B_d}(6 \times 1) \quad \boldsymbol{B_m}(6 \times 2) \right]. \tag{29}$$

The matrix $\boldsymbol{B}$ can be easily partitioned into two contributions. The matrix $\boldsymbol{B_d}$ is associated to the derivatives with respect of the dynamical model parameters, $\boldsymbol{C_d}$, and the matrix $\boldsymbol{B_m}$ is associated to the derivatives with respect of the measurements model. Since the measurements do not appear in the dynamical equations, we can conclude that $\boldsymbol{B_m} = 0$. The partial derivatives of F_4, F_5 and F_6 (components of $\boldsymbol{F}$ in Eq. (17)) with respect to Cr are derived from the solar radiation pressure acceleration and for a flat plate surface the derivative of the acceleration is:

$$\begin{Bmatrix} \frac{\partial F_4}{\partial Cr} \\ \frac{\partial F_5}{\partial Cr} \\ \frac{\partial F_6}{\partial Cr} \end{Bmatrix} = \frac{\partial \boldsymbol{a}_{srp}}{\partial Cr} = -\frac{K}{r_{ls}^2} \cos\theta \left(-\frac{\boldsymbol{r}_{ls}}{r_{ls}} + 2\cos\theta \hat{\boldsymbol{n}} \right) \tag{30}$$

with $\hat{\boldsymbol{n}}$ being the normal vector to the flat plate, pointing towards the Earth:

$$\hat{\boldsymbol{n}} = \frac{\boldsymbol{r}_{Earth}}{r_{Earth}}, \tag{31}$$

and θ being the angle between $\hat{\boldsymbol{n}}$ and the Sun-spacecraft direction $\boldsymbol{r}_{ls}$:

$$\cos\theta = \frac{\boldsymbol{r}_{ls} \cdot \boldsymbol{r}_{Earth}}{r_{ls} r_{Earth}} \tag{32}$$

ϵ is the reflectively parameter and K is a constant function of the spacecraft's property (mass/size) and Sun's luminosity. Further details in the definition of the SRP acceleration can be found in Appendix D. By knowing that $\frac{\partial F_1}{\partial Cr} = \frac{\partial F_2}{\partial Cr} = \frac{\partial F_3}{\partial Cr} = 0$, the matrix $\boldsymbol{B}$ can be rewritten as:

$$\boldsymbol{B} = \begin{bmatrix} \boldsymbol{0}_{3\times1} & \boldsymbol{0}_{3\times2} \\ \frac{\partial \boldsymbol{a}_{srp}}{\partial Cr} & \boldsymbol{0}_{3\times2} \end{bmatrix} \tag{33}$$

8.6 Sensitivity Matrix of the Consider Parameter Covariance Matrix ($\tilde{\boldsymbol{H}}_{ci}$)

The sensitivity matrix of the consider parameters is derived by linearizing the nonlinear measurement equations. From the definition given in Eq. (23), the sensitivity matrix of the consider parameter covariance matrix is given as:

$$\tilde{\boldsymbol{H}}_c = \begin{bmatrix} \frac{\partial \rho}{\partial Cr} & \frac{\partial \rho}{\partial \Delta\alpha} & \frac{\partial \rho}{\partial \Delta\delta} \\ \frac{\partial \dot{\rho}}{\partial Cr} & \frac{\partial \dot{\rho}}{\partial \Delta\alpha} & \frac{\partial \dot{\rho}}{\partial \Delta\delta} \\ \frac{\partial \alpha}{\partial Cr} & \frac{\partial \alpha}{\partial \Delta\alpha} & \frac{\partial \alpha}{\partial \Delta\delta} \\ \frac{\partial \delta}{\partial Cr} & \frac{\partial \delta}{\partial \Delta\alpha} & \frac{\partial \delta}{\partial \Delta\delta} \end{bmatrix} = \begin{bmatrix} 0 & 0 & 0 \\ 0 & 0 & 0 \\ 0 & 1 & 0 \\ 0 & 0 & 1 \end{bmatrix}. \tag{34}$$

8.7 Consider Parameters Covariance Matrix ($\boldsymbol{P}_c$): Least Square Batch Filter

The consider parameters covariance matrix, $\boldsymbol{P}_c$, is larger than the noise-only covariance, $\boldsymbol{P}_x$. By adopting a large number of measurements, the impact of the data noise is effectively averaged out and the uncertainty of the estimated parameters is decreased. The consider parameters are assumed to be constant throughout a single orbit determination but affected by a given uncertainty. The matrix $\boldsymbol{P}_c$ does not decrease with the increasing in the data rate, but it is essentially constant for a given data arc and tracking configuration. The consider covariance batch filter is suited for assessing the impact of systematic errors in the orbit determination process. For the case of the consider parameters, the covariance matrix is computed as (Montenbruck and Gill 2005):

$$\boldsymbol{P}_c = \boldsymbol{P}_x + (\boldsymbol{P}_x \boldsymbol{H}^T \boldsymbol{W})(\boldsymbol{H}_c \boldsymbol{C}_c \boldsymbol{H}_c^T)(\boldsymbol{P}_x \boldsymbol{H}^T \boldsymbol{W})^T. \tag{35}$$

The noise-only covariance matrix, $\boldsymbol{P}_x$, is given by:

$$\boldsymbol{P}_x = \left(\sum_i \boldsymbol{H}_i^T \boldsymbol{W}_i \boldsymbol{H}_i\right)^{-1} = \left(\sum_i \boldsymbol{P}_i\right)^{-1} \tag{36}$$

where the weight matrix, $\boldsymbol{W}_i$, is defined as:

$$\boldsymbol{W}_i = \begin{bmatrix} \sigma_\rho^{-2}(t_i) & 0 & 0 & 0 \\ 0 & \sigma_{\dot{\rho}}^{-2}(t_i) & 0 & 0 \\ 0 & 0 & \sigma_\alpha^{-2}(t_i) & 0 \\ 0 & 0 & 0 & \sigma_\delta^{-2}(t_i) \end{bmatrix}. \tag{37}$$

We can now derive the following matrices as:

$$\boldsymbol{H}^T \boldsymbol{W} = \sum_i \boldsymbol{H}_i^T \boldsymbol{W}_i = \sum_i \boldsymbol{HW}_i, \tag{38}$$

and

$$\boldsymbol{H}_c \boldsymbol{C}_c \boldsymbol{H}_c^T = \sum_i \boldsymbol{H}_{ci} \boldsymbol{C}_{ci} \boldsymbol{H}_{ci}^T = \sum_i \boldsymbol{HCH}_i. \tag{39}$$

The inverse of the weight matrix associated to the constraint parameters is provided by:

$$\boldsymbol{C}_{ci} = \begin{bmatrix} \sigma_{Cr}^2(t_i) & 0 & 0 \\ 0 & \sigma_{\Delta\alpha}^2(t_i) & 0 \\ 0 & 0 & \sigma_{\Delta\delta}^2(t_i) \end{bmatrix}. \tag{40}$$

Note that, the covariance matrix was computed in J2000EQ-Ry but it can be transformed in the HP reference frame.

8.8 Covariance Analysis

The covariance matrix along the reference conjunction trajectory can be computed as a function of time as follow:

$$\bar{\boldsymbol{P}}(t_{i+1}) = \left[\left(\boldsymbol{\Phi}(t_{i+1}, t_i) \bar{\boldsymbol{P}}(t_i) \boldsymbol{\Phi}^T(t_{i+1}, t_i) \right)^{-1} + \boldsymbol{P}_c^{-1}(t_{i+1}) \right]^{-1} + P_n(t_{i+1}) \tag{41}$$

with $\boldsymbol{\Phi}(t_i, t_i) = \boldsymbol{I}$. Note that the state transition matrix is used to update the time of the covariance matrix from t_i to t_{i+1}. We also distinguished between the time before and after the maneuver where the effect of the process noise (ΔV execution error) is given by $\boldsymbol{P}_n$ that was previously introduced in Eq. (16) and here transformed in J2000EQ-Ry coordinates. The effect of the initial knowledge covariance matrix is included in the term $\bar{\boldsymbol{P}}(t_i)$ while the effect of the navigation at time t_{i+1} is included in the matrix $\boldsymbol{P}_c(t_{i+1})$. Note that the effect of the navigation at t_i is given in the term $\bar{\boldsymbol{P}}(t_i)$. Once the covariances before and after the ΔV maneuver at COI, TCM1, TCM2 and HRM are given, it is possible to compute the stochastic ΔV (guidance). Figure 25 shows the standard deviation expressed in the HP frame and projected to the final HRM epoch for both the positions and velocities. The dashed gray vertical lines highlight the TCM1 (-29 days to HRM) and the TCM2 (-4 days to HRM) epochs. The red dots show the effect of the execution error ΔV. As one can see, the effect of the navigation before TCM1 (Leg 1) and TCM2 (Leg 2) aims to reduce the standard deviation error at HRM.

8.9 Semi-analytic Stochastic ΔV Method

For the statistical analysis of control maneuvers, we follow the idea presented in Renaultand and Scheeres (2003). A similar approach has been used for the design of the TCMs during the Hayabusa2's approach phase (Tsuda et al. 2013).

The stochastic ΔV can be computed analytically following the definition of the state transition matrix. At time t_i, a manoeuvre ΔV_i is executed to null the error in position at time t_{HRM}, and a manoeuvre ΔV_{HRM} is scheduled at time t_{HRM} to null the error in velocity

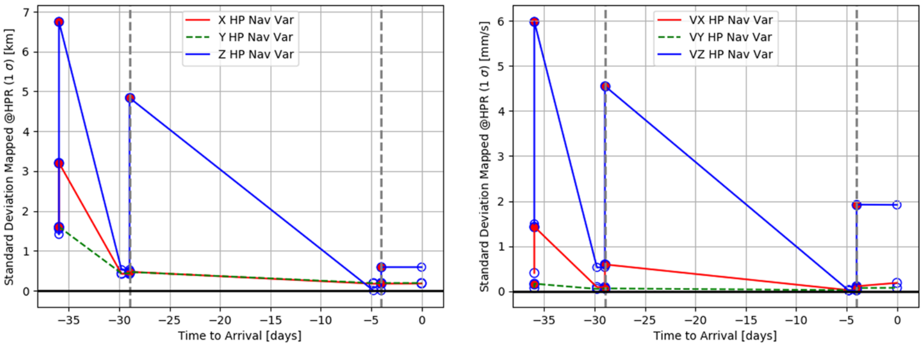

(a) Variance in position.

(b) Variance in velocity.

Fig. 25 Variance in position and velocity in the HP frame projected at HRM epoch: ONC-W1 case

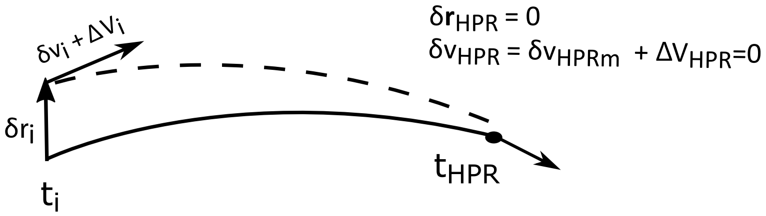

Fig. 26 Schematic representation of the shooting method for the semi-analytic computation of the stochastic ΔV

at HRM. The principle of the semi-analytic computation of the stochastic ΔVs is shown in Fig. 26. Therefore, we can write the following formulas:

$$\begin{Bmatrix} \delta \boldsymbol{r}_{HRM_m} \\ \delta \boldsymbol{v}_{HRM_m} \end{Bmatrix} = \begin{bmatrix} \boldsymbol{\Phi}_{11} & \boldsymbol{\Phi}_{12} \\ \boldsymbol{\Phi}_{21} & \boldsymbol{\Phi}_{22} \end{bmatrix}_{(t_{HRM}, t_i)} \begin{Bmatrix} \delta \boldsymbol{r}_i \\ \delta \boldsymbol{v}_i + \Delta V_i \end{Bmatrix} \tag{42}$$

and

$$\begin{Bmatrix} \delta \boldsymbol{r}_{HRM} \\ \delta \boldsymbol{v}_{HRM} \end{Bmatrix} = \begin{bmatrix} \boldsymbol{\Phi}_{11} & \boldsymbol{\Phi}_{12} \\ \boldsymbol{\Phi}_{21} & \boldsymbol{\Phi}_{22} \end{bmatrix}_{(t_{HRM}, t_i)} \begin{Bmatrix} \delta \boldsymbol{r}_i \\ \delta \boldsymbol{v}_i + \Delta V_i \end{Bmatrix} + \begin{Bmatrix} \boldsymbol{0} \\ \Delta V_{HRM} \end{Bmatrix}. \tag{43}$$

Given Eq. (43), the objective is to have $\delta \boldsymbol{r}_{HRM} = \delta \boldsymbol{v}_{HRM} = \boldsymbol{0}$. Therefore, Eq. (43) can be rewritten as:

$$\begin{cases} \boldsymbol{\Phi}_{11}(t_{HRM}, t_i)\delta \boldsymbol{r}_i + \boldsymbol{\Phi}_{12}(t_{HRM}, t_i)\delta \boldsymbol{v}_i + \boldsymbol{\Phi}_{12}(t_{HRM}, t_i)\Delta V_i & = \boldsymbol{0} \\ \boldsymbol{\Phi}_{21}(t_{HRM}, t_i)\delta \boldsymbol{r}_i + \boldsymbol{\Phi}_{22}(t_{HRM}, t_i)\delta \boldsymbol{v}_i + \boldsymbol{\Phi}_{22}(t_{HRM}, t_i)\Delta V_i + \Delta V_{HRM} & = \boldsymbol{0}. \end{cases} \tag{44}$$

By rearranging Eq. (44) as an explicit function of the stochastic ΔV, we get:

$$\begin{Bmatrix} \Delta V_i \\ \Delta V_{HRM} \end{Bmatrix} = \begin{bmatrix} -\boldsymbol{\Phi}_{12}^{-1}\boldsymbol{\Phi}_{11} & -\boldsymbol{I} \\ \boldsymbol{\Phi}_{22}\boldsymbol{\Phi}_{12}^{-1}\boldsymbol{\Phi}_{11} - \boldsymbol{\Phi}_{21} & \boldsymbol{0} \end{bmatrix}_{(t_{HRM}, t_i)} \begin{Bmatrix} \delta \boldsymbol{r}_i \\ \delta \boldsymbol{v}_i \end{Bmatrix} \tag{45}$$

so that in a compact form we have:

$$\Delta\boldsymbol{V} = \boldsymbol{Q}(t_{HRM}, t_i)\delta\boldsymbol{x}_i. \tag{46}$$

The covariance matrix of the stochastic ΔV is given by:

$$\boldsymbol{P}_{\Delta V} = E[\Delta\boldsymbol{V}\Delta\boldsymbol{V}^T] = \boldsymbol{Q}(t_{HRM}, t_i)E[\delta\boldsymbol{x}_i\delta\boldsymbol{x}_i^T]\boldsymbol{Q}^T(t_{HRM}, t_i) \tag{47}$$

and we recognise that $E[\Delta\boldsymbol{V}\Delta\boldsymbol{V}^T]$ is the covariance matrix in Eq. (41):

$$\boldsymbol{P}_{\Delta V} = \boldsymbol{Q}(t_{HRM}, t_i)\bar{\boldsymbol{P}}_i(t_i)\boldsymbol{Q}^T(t_{HRM}, t_i). \tag{48}$$

In Eq. (48), t_i is the time of the maneuver (e.g. COI, TCM1 and TCM2) and the covariance matrix $\bar{\boldsymbol{P}}_i(t_i)$ is computed as in E. (41). The diagonal of the covariance matrix provides the standard deviation of the stochastic ΔV:

$$diag(\boldsymbol{P}_{\Delta V}) = \begin{bmatrix} \sigma^2_{V_{xi}} & 0 & 0 & 0 & 0 & 0 \\ 0 & \sigma^2_{V_{yi}} & 0 & 0 & 0 & 0 \\ 0 & 0 & \sigma^2_{V_{zi}} & 0 & 0 & 0 \\ 0 & 0 & 0 & \sigma^2_{V_{x,HRM}} & 0 & 0 \\ 0 & 0 & 0 & 0 & \sigma^2_{V_{y,HRM}} & 0 \\ 0 & 0 & 0 & 0 & 0 & \sigma^2_{V_{z,HRM}} \end{bmatrix} \tag{49}$$

and we can now separate the covariance matrix of the stochastic ΔV at time t_i and the one at t_{HRM} so that we can write in a compact way:

$$diag(\boldsymbol{P}_{\Delta V}) = \begin{bmatrix} \boldsymbol{P}^{(3\times3)}_{\Delta \boldsymbol{V}_{i,\ J2000}}(t_i) & \boldsymbol{0} \\ \boldsymbol{0} & \boldsymbol{P}^{(3\times3)}_{\Delta \boldsymbol{V}_{HRM,\ J2000}}(t_{HRM}) \end{bmatrix}. \tag{50}$$

We are interested only in the standard deviation at time t_i, $\boldsymbol{P}^{(3\times3)}_{\Delta \boldsymbol{V}_{i,J2000}}(t_i)$. Figure 27 shows the results of the covariance analysis for the deterministic and the stochastic ΔVs in each components of the HP reference frame. Note that due to the mounting direction of the thrusters attached to the body of the spacecraft, we have to account for a thrust loss factor of $\cos(75°)^{-1}$ in ΔVs given along the y_{hp} coordinate. Given the linear covariance analysis, Fig. 28 shows an example of estimated trajectory (in red) vs the ayu nominal trajectory (in blue).

8.10 Monte Carlo Analysis in the Nonlinear System

In this section, we verified that the covariance matrix propagated from COI to TCM2 (no navigation) returns the same stochastic ΔV in both the previously presented semi-analytic method (Fig. 29.b) and the Monte Carlo method for the nonlinear system (Gordon 1991) (Fig. 29.a). For the Monte Carlo analysis, we performed a simple shooting between TCM2 and HRM to determine the standard deviation of the ΔV at TCM2 under the effect of nonlinearities. Table 10 shows the results of the two analysis compared. Both methods give similar solutions showing that the semi-analytic method is reliable under the effect of nonlinearities. We also demonstrated that our shooting method (optNEAR) can control the spacecraft within a 99% confidence criterion as shown in Table 10 and in Fig. 29.a (red trajectories).

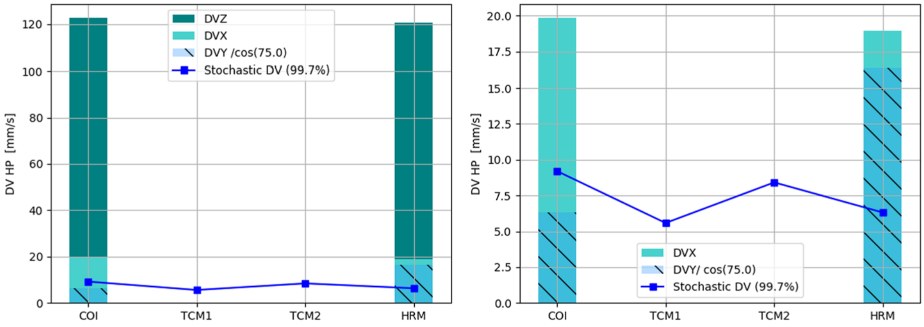

(a) X_{HP},Y_{HP} and Z_{HP} components. (b) X_{HP} and Y_{HP} components.

Fig. 27 Deterministic and stochastic ΔV in the HP frame

Fig. 28 Design trajectory (blue) and estimated trajectory (red) in J2000EQ frame for the case of ONC-W1

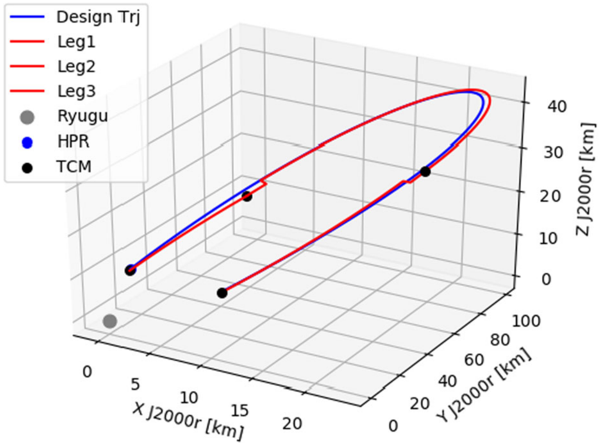

Table 10 Comparison of the stochastic ΔV at TCM2 between the Monte Carlo solution and the semi-analytic method

Solution at TCM2	$\sigma_{\Delta V X_{HP}}$ [mm/s]	$\sigma_{\Delta V Y_{HP}}$ [mm/s]	$\sigma_{\Delta V Z_{HP}}$ [mm/s]
Monte Carlo	20.81	20.71	29.47
Semi-analytic method	20.84	20.77	29.84

9 Conclusions

In this article, we have shown the design of the ayu conjunction trajectory for hovering satellite around minor bodies. The case of the Hayabusa2 mission trajectory planning was presented. The ayu trajectory is a low energy transfer trajectory designed in the Hill reference frame. It requires two deterministic ΔVs (COI/HRM) with overall fuel cost of less than 1 m/s. Uncertainties in the insertion ΔV at COI affects the overall ΔV_x at HRM. Under contingency scenario at HRM, a recovery trajectory can be rescheduled after one day from the missed HRM maneuver. The effect of the BOX-A's initial knowledge navigation error at COI requires at least one TCM maneuver after deep conjunction (SEP angle $\sim 0°$). To

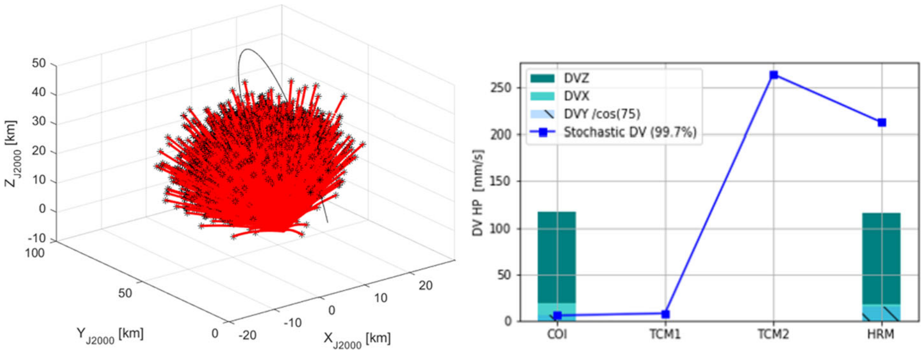

(a) Monte Carlo Method. (b) Semi-Analytic Method.

Fig. 29 Deterministic and stochastic ΔV in the HP frame

be conservative, at least two TCMs maneuvers should be scheduled during the operations. The effect of uncertainties in the observations and dynamical model are investigated and the stochastic ΔVs are computed using a semi-analytic formulation. When compared to the nonlinear Monte Carlo method, we concluded that the semi-analytic formula works well. Moreover, we are confident that the shooting method developed in optNEAR works well for the ΔV planning during the superior solar conjunction mission operation.

Acknowledgements The authors would like to thank the Hayabusa2 Project Team. This research was developed at the Institute of Space and Astronautical Science/JAXA. S. Soldini would like to thank the JAXA's Aerospace Project Research Associate program (2017-2019) and the Hayabusa2 project for funding this research.

Appendix A: Transformations Between the Hill and the HP Reference Frames

Given the position, $\boldsymbol{r}_{Hill}$, and velocity, $\boldsymbol{v}_{Hill}$, in the Hill coordinates, the following set of equations transforms the spacecraft's state vector in the HP coordinates:

$$\begin{cases} r_{hp} &= \boldsymbol{C}_{HP}^{\intercal}\boldsymbol{C}\boldsymbol{r}_{Hill} \\ \boldsymbol{v}_{hp} &= \boldsymbol{C}_{HP}^{\intercal}\boldsymbol{C}\boldsymbol{v}_{Hill} + \boldsymbol{C}_{HP}^{\intercal}\dot{\boldsymbol{C}}\boldsymbol{r}_{Hill} - \boldsymbol{C}_{HP}^{\intercal}\dot{\boldsymbol{C}}_{HP}\boldsymbol{r}_{HP}. \end{cases} \tag{51}$$

In Eq. (51), $\boldsymbol{C}_{HP}$ is the transformation matrix that takes coordinates in the HP reference frame (3) to coordinates in J2000EQ-Ry reference frame (2) introduced in Sect. 2. The

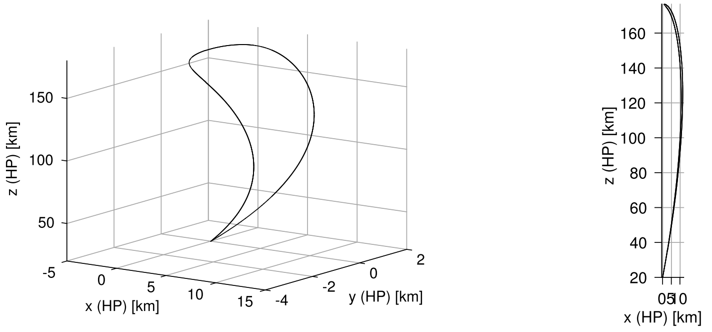

(a) 3D view. (b) 2D view.

Fig. 30 Conjunction trajectory as seen from the HP Frame

derivative of $\boldsymbol{C}_{HP}$ is given by:

$$\dot{\boldsymbol{C}}_{HP} = [\dot{\hat{\boldsymbol{r}}}_1|\dot{\hat{\boldsymbol{r}}}_2|\dot{\hat{\boldsymbol{r}}}_3], \tag{52}$$

and

1) $\dot{\hat{\boldsymbol{r}}}_3 = \frac{\boldsymbol{v}_{Earth}}{|\boldsymbol{r}_{Earth}|} - \frac{(\boldsymbol{r}_{Earth}\bullet\boldsymbol{v}_{Earth})}{|\boldsymbol{r}_{Earth}|}\frac{\boldsymbol{r}_{Earth}}{|\boldsymbol{r}_{Earth}|^2}$;

2) $\dot{\hat{\boldsymbol{r}}}_2 = \frac{\boldsymbol{v}_{Earth}\times\boldsymbol{r}_{Sun}}{|\boldsymbol{r}_{Earth}\times\boldsymbol{r}_{Sun}|} + \frac{\boldsymbol{r}_{Earth}\times\boldsymbol{v}_{Sun}}{|\boldsymbol{r}_{Earth}\times\boldsymbol{r}_{Sun}|} - \frac{\boldsymbol{r}_{Earth}\times\boldsymbol{r}_{Sun}}{|\boldsymbol{r}_{Earth}\times\boldsymbol{r}_{Sun}|^2}\left(\frac{(\boldsymbol{r}_{Earth}\times\boldsymbol{r}_{Sun})\bullet((\boldsymbol{v}_{Earth}\times\boldsymbol{r}_{Sun})+(\boldsymbol{r}_{Earth}\times\boldsymbol{v}_{Sun}))}{|\boldsymbol{r}_{Earth}\times\boldsymbol{r}_{Sun}|}\right)$;

Note that, it is possible to derive the following expressions:

$$\boldsymbol{r}_{Earth}\times\boldsymbol{r}_{Sun} = \begin{vmatrix} \hat{x} & \hat{y} & \hat{z} \\ x_e & y_e & z_e \\ x_s & y_s & z_s \end{vmatrix} = \begin{Bmatrix} y_e z_s - z_e y_s \\ z_e x_s - z_s x_e \\ x_e y_s - x_s y_e \end{Bmatrix} \tag{53}$$

with

$$|\boldsymbol{r}_{Earth}\times\boldsymbol{r}_{Sun}| = \sqrt{(y_e z_s - z_e y_s)^2 + (z_e x_s - z_s x_e)^2 + (x_e y_s - x_s y_e)^2} \tag{54}$$

and

$$\begin{aligned} &\frac{d}{dt}|\boldsymbol{r}_{Earth}\times\boldsymbol{r}_{Sun}| \\ &= \frac{1}{|\boldsymbol{r}_{Earth}\times\boldsymbol{r}_{Sun}|}\left(\begin{Bmatrix} y_e z_s - z_e y_s \\ z_e x_s - z_s x_e \\ x_e y_s - x_s y_e \end{Bmatrix} \bullet \begin{Bmatrix} \dot{y}_e z_s + y_e \dot{z}_s - z_e \dot{y}_s - \dot{z}_e y_s \\ \dot{z}_e x_s + z_e \dot{x}_s - \dot{z}_s x_e - z_s \dot{x}_e \\ \dot{x}_e y_s + x_e \dot{y}_s - \dot{x}_s y_e - x_s \dot{y}_e \end{Bmatrix}\right) \\ &= \frac{1}{|\boldsymbol{r}_{Earth}\times\boldsymbol{r}_{Sun}|}\left[(\boldsymbol{r}_{Earth}\times\boldsymbol{r}_{Sun})\bullet\left(\begin{Bmatrix} \dot{y}_e z_s - \dot{z}_e y_s \\ \dot{z}_e x_s - z_s \dot{x}_e \\ \dot{x}_e y_s - x_s \dot{y}_e \end{Bmatrix} + \begin{Bmatrix} y_e \dot{z}_s - z_e \dot{y}_s \\ z_e \dot{x}_s - \dot{z}_s x_e \\ x_e \dot{y}_s - \dot{x}_s y_e \end{Bmatrix}\right)\right] \\ &= \frac{(\boldsymbol{r}_{Earth}\times\boldsymbol{r}_{Sun})\bullet((\boldsymbol{v}_{Earth}\times\boldsymbol{r}_{Sun})+(\boldsymbol{r}_{Earth}\times\boldsymbol{v}_{Sun}))}{|\boldsymbol{r}_{Earth}\times\boldsymbol{r}_{Sun}|} \end{aligned} \tag{55}$$

3) $\dot{\hat{\boldsymbol{r}}}_1 = \left(\dot{\hat{\boldsymbol{r}}}_2\times\hat{\boldsymbol{r}}_3\right) + \left(\hat{\boldsymbol{r}}_2\times\dot{\hat{\boldsymbol{r}}}_3\right)$.

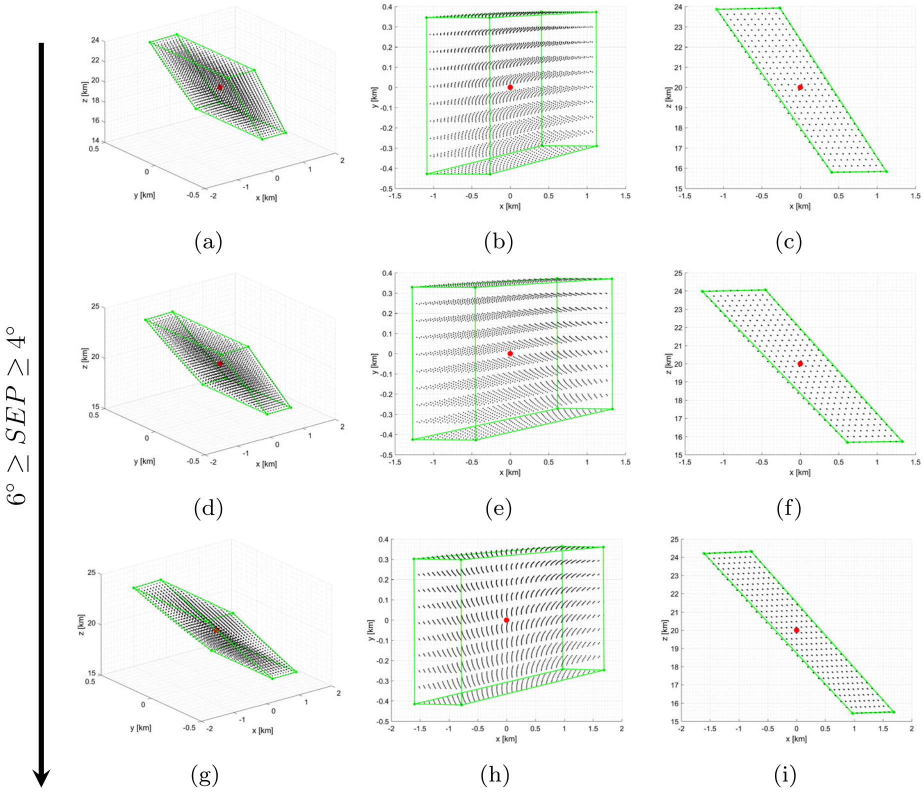

Fig. 31 Dispersion in position at HRM: $\mu_a = 11\ \mathrm{m}^3/\mathrm{s}^2$

The rotation matrix $\boldsymbol{C}$ takes coordinates in the Hill reference frame (1) (in Sect. 2) to coordinates in J2000EQ-Ry reference frame (2) (in Sect. 2):

$$\boldsymbol{C} = [\hat{\boldsymbol{c}}_1 | \hat{\boldsymbol{c}}_2 | \hat{\boldsymbol{c}}_3], \tag{56}$$

where

1) $\hat{\boldsymbol{c}}_1 = \frac{\boldsymbol{r}_a}{|\boldsymbol{r}_a|}$;
2) $\hat{\boldsymbol{c}}_3 = \frac{\boldsymbol{h}}{|\boldsymbol{h}|} = \frac{\boldsymbol{r}_a \times \boldsymbol{v}_a}{|\boldsymbol{r}_a \times \boldsymbol{v}_a|}$;
3) $\hat{\boldsymbol{c}}_2 = \frac{\hat{\boldsymbol{c}}_3 \times \hat{\boldsymbol{c}}_1}{|\hat{\boldsymbol{c}}_3 \times \hat{\boldsymbol{c}}_1|}$,

where $\boldsymbol{r}_a$ and $\boldsymbol{v}_a$ are the position and the velocity of the asteroid with respect to the Sun.[5] We assumed that $\dot{\boldsymbol{C}} = \boldsymbol{0}$.

Figure 30 shows the ayu trajectory in the HP reference frame. As the ayu trajectory is designed to departure from HP position (20 km altitude in the z-hp coordinate) at COI and return at HP at HRM, the ayu trajectory appears as a periodic orbit in the HP reference frame.

---

[5] $\boldsymbol{r}_a = \boldsymbol{r}_{Ryugu|_{J200EQ}}$.

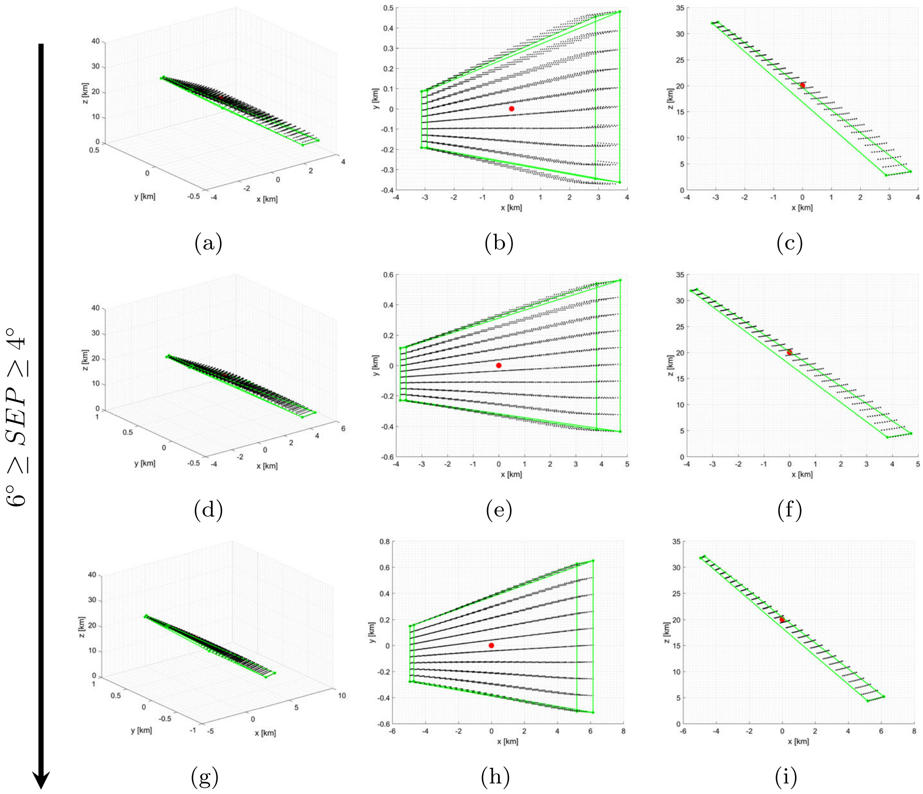

(a) (b) (c)

(d) (e) (f)

(g) (h) (i)

Fig. 32 Dispersion in position at HRM: $\mu_a = 92\ \mathrm{m}^3/\mathrm{s}^2$

Appendix B: Uncertainty Analysis in Position

Figure 31 shows that all the solutions inside BOX-A at COI are bounded inside the box at HRM therefore, it makes sense to limit the analysis to the corner solutions of BOX-A for $\mu_a = 11\ \mathrm{m}^3/\mathrm{s}^2$.

Fig. 32 shows that all the solutions inside BOX-A at COI are bounded inside the box at HRM therefore, it makes sense to limit the analysis to the corner solutions of BOX-A for $\mu_a = 92\ \mathrm{m}^3/\mathrm{s}^2$. This behaviour seems to hold true for all the values in μ_a analysed.

Appendix C: Uncertainty Analysis in Velocity

Figure 33 shows the Gaussian distribution in position at HRM for $3\sigma = 7$ mm/s of uncertainty at COI while Fig. 34 shows the distribution of the arrival velocity at HRM. Tables 11 and 12 show the 1σ error in both the final position (Fig. 33) and velocity (Fig. 34) at HRM for all the six cases. The maximum errors are in the Hill x-coordinate for solution c in Fig. 33–34 with a 3σ error of 16 km in position and 4.75 cm/s.

Initial navigation errors at around 7 mm/s requires at least one TCM after the deep conjunction point to compensate of the large errors in position and velocity at HRM.

Initial navigation errors at around 1 cm/s requires at least one TCM after the deep conjunction point to compensate of the large errors in position and velocity at HRM.

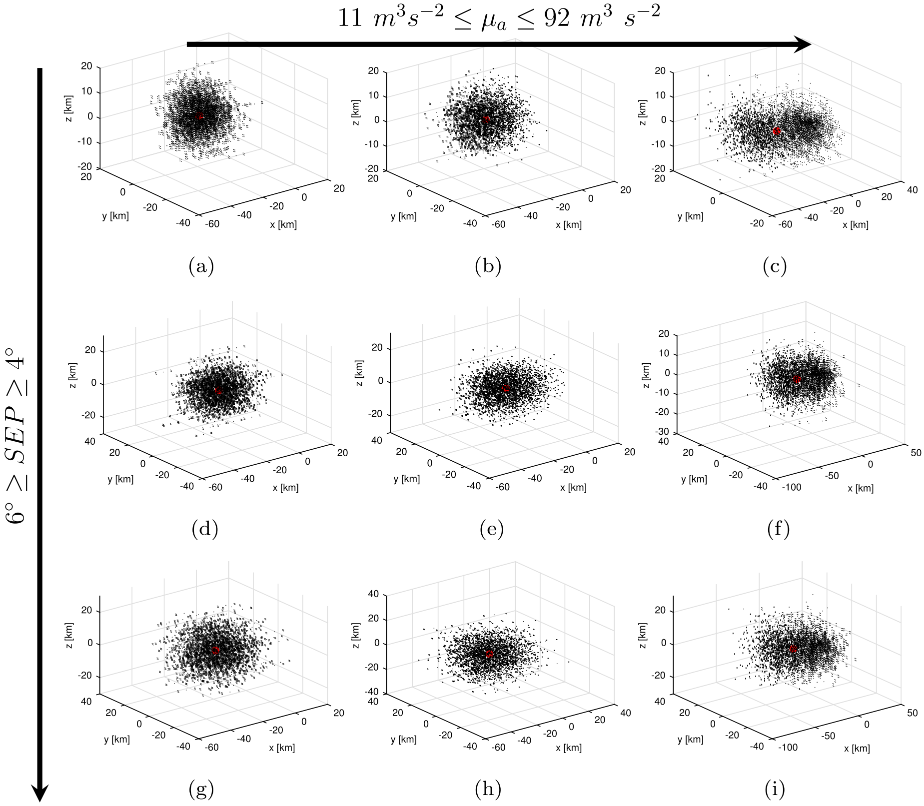

Fig. 33 Positions at HRM with HP-NAV error of $3\sigma = 7$ mm/s at COI

Table 11 Reference position at HRM ± 1σ with $3\sigma = 7$ mm/s at COI

SEP [°]	μ_a [m^3/s^2]		
	11	32	92
4	a) $x = -19.97 \pm 7.61$ km $y = -0.959 \pm 5.84$ km $z = 0.320 \pm 5.78$ km	b) $x = -19.97 \pm 8.99$ km $y = -0.959 \pm 5.87$ km $z = 0.320 \pm 5.69$ km	c) $x = -19.97 \pm 15.68$ km $y = -0.959 \pm 5.398$ km $z = 0.320 \pm 5.063$ km
5	d) $x = -19.96 \pm 8.88$ km $y = -1.164 \pm 6.85$ km $z = 0.362 \pm 6.86$ km	e) $x = -19.96 \pm 10.4$ km $y = -1.164 \pm 7.06$ km $z = 0.362 \pm 6.61$ km	f) $x = -19.96 \pm 16.14$ km $y = -1.164 \pm 6.869$ km $z = 0.362 \pm 6.137$ km
6	g) $x = -19.94 \pm 10.5$ km $y = -1.437 \pm 8.24$ km $z = 0.415 \pm 8.47$ km	h) $x = -19.90 \pm 12.1$ km $y = -1.437 \pm 8.77$ km $z = 0.415 \pm 8.51$ km	i) $x = -19.94 \pm 17.06$ km $y = -1.438 \pm 8.660$ km $z = 0.415 \pm 7.942$ km

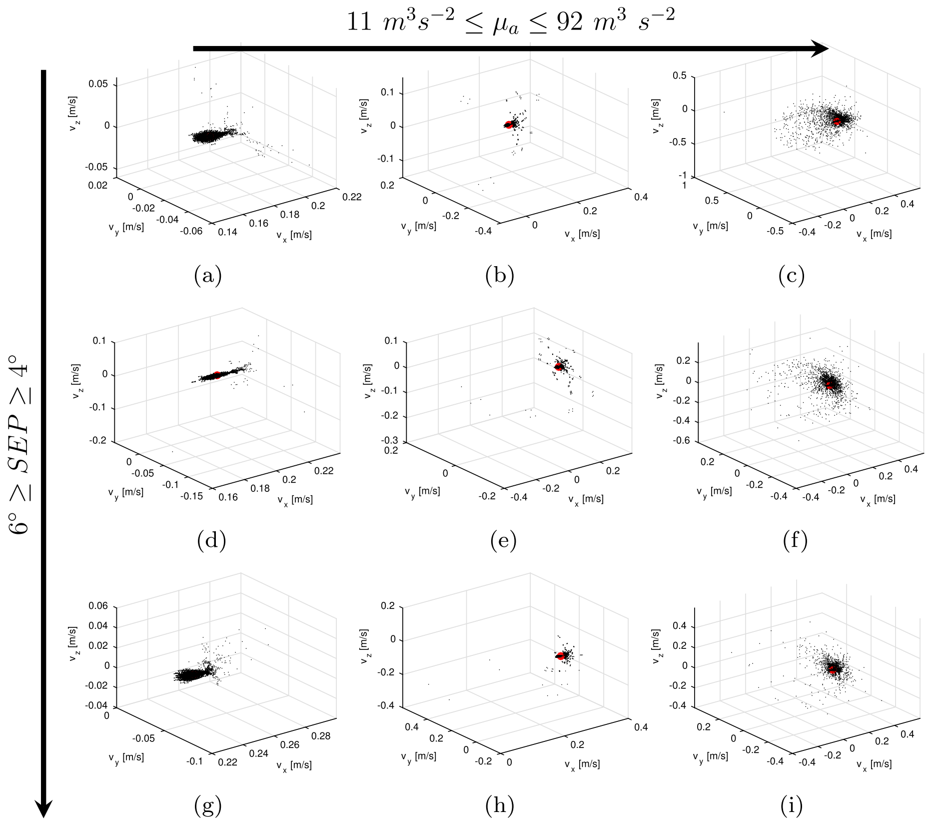

Fig. 34 Velocities at HRM with HP-NAV error of $3\sigma = 7$ mm/s at COI

Table 12 Reference velocity at HRM ± 1σ with $3\sigma = 7$ mm/s at COI

SEP [°]	μ_a [m^3/s^2]		
	11	32	92
4	a) $v_x = 17.03 \pm 0.44$ cm/s $v_y = -1.854 \pm 0.25$ cm/s $v_z = 0.014 \pm 0.23$ cm/s	b) $v_x = 17.66 \pm 0.97$ cm/s $v_y = -1.889 \pm 0.67$ cm/s $v_z = 0.009 \pm 0.58$ cm/s	c) $v_x = 19.34 \pm 4.75$ cm/s $v_y = -1.985 \pm 4.78$ cm/s $v_z = -0.003 \pm 4.47$ cm/s
5	d) $v_x = 20.10 \pm 0.43$ cm/s $v_y = -2.600 \pm 0.25$ cm/s $v_z = 0.014 \pm 0.33$ cm/s	e) $v_x = 20.64 \pm 1.19$ cm/s $v_y = -2.634 \pm 0.76$ cm/s $v_z = 0.010 \pm 0.82$ cm/s	f) $v_x = 22.11 \pm 3.44$ cm/s $v_y = -2.725 \pm 3.79$ cm/s $v_z = -0.003 \pm 3.71$ cm/s
6	g) $v_x = 24.52 \pm 0.42$ cm/s $v_y = -3.937 \pm 0.25$ cm/s $v_z = 0.014 \pm 0.23$ cm/s	h) $v_x = 24.96 \pm 0.75$ cm/s $v_y = -3.968 \pm 1.10$ cm/s $v_z = 0.010 \pm 0.92$ cm/s	i) $v_x = 26.18 \pm 2.56$ cm/s $v_y = -4.055 \pm 2.69$ cm/s $v_z = -0.002 \pm 2.68$ cm/s

Figure 34 shows the Gaussian distribution in position at HRM for $3\sigma = 1$ cm/s of uncertainty at COI while Fig. 36 shows the distribution of the arrival velocity at HRM. Tables 13 and 14 show the 1σ error in both the final position (Fig. 35) and velocity (Fig. 36) at HRM for all the six cases. The maximum errors are in the Hill x-coordinate for solution c in Fig. 35–36 with a 3σ error of 18 km in position and 4.63 cm/s.

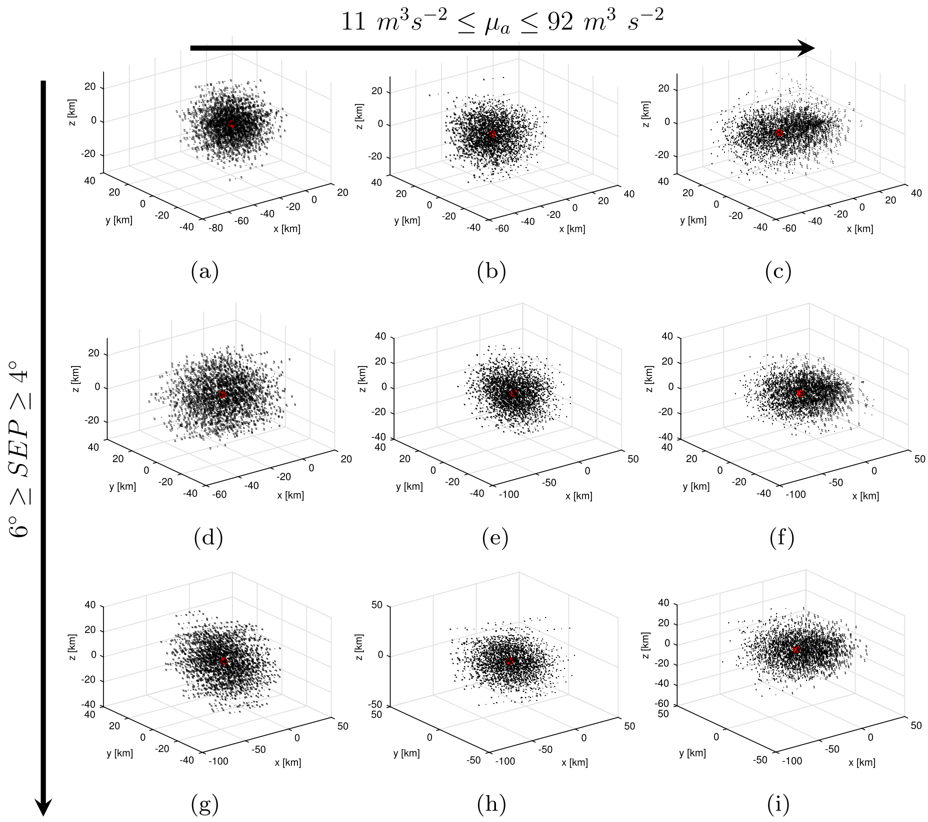

Fig. 35 Positions at HRM with HP-NAV error of $3\sigma = 1$ cm/s at COI

Table 13 Reference position at HRM ± 1σ with $3\sigma = 1$ cm/s at COI

SEP [°]	μ_a [m^3/s^2]					
	11		32		92	
4	a)	$x = -19.97 \pm 10.08$ km $y = -0.960 \pm 8.420$ km $z = 0.320 \pm 8.140$ km	b)	$x = -19.97 \pm 11.26$ km $y = -0.960 \pm 8.230$ km $z = 0.320 \pm 8.330$ km	c)	$x = -19.97 \pm 17.26$ km $y = -0.960 \pm 7.780$ km $z = 0.320 \pm 7.170$ km
5	d)	$x = -19.96 \pm 12.18$ km $y = -1.160 \pm 10.11$ km $z = 0.362 \pm 9.880$ km	e)	$x = -19.96 \pm 13.11$ km $y = -1.160 \pm 10.14$ km $z = 0.362 \pm 10.13$ km	f)	$x = -19.96 \pm 18.53$ km $y = -1.160 \pm 9.724$ km $z = 0.362 \pm 8.881$ km
6	g)	$x = -19.94 \pm 15.10$ km $y = -1.437 \pm 12.23$ km $z = 0.415 \pm 12.26$ km	h)	$x = -19.94 \pm 16.28$ km $y = -1.437 \pm 12.45$ km $z = 0.415 \pm 12.07$ km	i)	$x = -19.94 \pm 19.82$ km $y = -1.437 \pm 12.49$ km $z = 0.415 \pm 11.46$ km

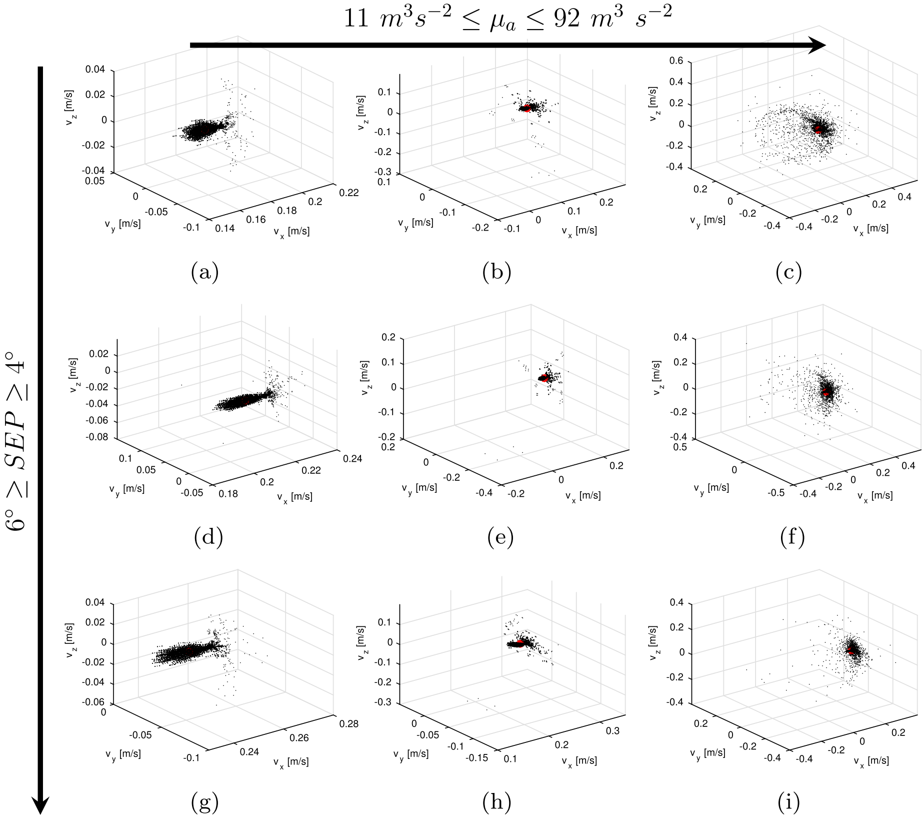

Fig. 36 Velocities at HRM with HP-NAV error of $3\sigma = 1$ cm/s at COI

Table 14 Reference velocity at HRM ± 1σ with $3\sigma = 1$ cm/s at COI

SEP [°]	μ_a [m^3/s^2]		
	11	32	92
4	a) $v_x = 17.03 \pm 0.55$ cm/s $v_y = -1.854 \pm 0.34$ cm/s $v_z = 0.014 \pm 0.31$ cm/s	b) $v_x = 17.66 \pm 0.98$ cm/s $v_y = -1.889 \pm 0.75$ cm/s $v_z = 0.009 \pm 0.94$ cm/s	c) $v_x = 19.34 \pm 4.63$ cm/s $v_y = -1.985 \pm 4.01$ cm/s $v_z = -0.003 \pm 4.24$ cm/s
5	d) $v_x = 20.10 \pm 0.54$ cm/s $v_y = -2.600 \pm 0.37$ cm/s $v_z = 0.014 \pm 0.31$ cm/s	e) $v_x = 20.64 \pm 1.04$ cm/s $v_y = -2.634 \pm 0.91$ cm/s $v_z = 0.010 \pm 0.75$ cm/s	f) $v_x = 22.11 \pm 2.86$ cm/s $v_y = -2.725 \pm 3.36$ cm/s $v_z = -0.002 \pm 3.02$ cm/s
6	g) $v_x = 24.52 \pm 0.52$ cm/s $v_y = -3.937 \pm 0.37$ cm/s $v_z = 0.014 \pm 0.31$ cm/s	h) $v_x = 24.96 \pm 0.75$ cm/s $v_y = -3.968 \pm 0.59$ cm/s $v_z = 0.010 \pm 0.73$ cm/s	i) $v_x = 26.18 \pm 2.06$ cm/s $v_y = -4.055 \pm 2.31$ cm/s $v_z = -0.002 \pm 2.39$ cm/s

Appendix D: optNEAR Tool - N-Body Propagator in J2000EQ-Ry Coordinates

The dynamics of the optNEAR propagator are written centred at Ryugu. optNEAR makes use of third party NASA's SPICE Toolkit to download the ephemeris of Ryugu, all Planets, Earth, Moon and Sun. The effect of SRP is also taken into account and Eq. (17) is defined as:

$$\begin{Bmatrix} \dot{X} \\ \dot{Y} \\ \dot{Z} \\ \ddot{X} \\ \ddot{Y} \\ \ddot{Z} \end{Bmatrix} = \begin{bmatrix} \dot{X} \\ \dot{Y} \\ \dot{Z} \\ -\frac{\mu_a}{r^3} X + \sum_{j=1}^{NP_j} a_P|_{x_j} + a_{srp}|_x \\ -\frac{\mu_a}{r^3} Y + \sum_{j=1}^{NP_j} a_P|_{y_j} + a_{srp}|_y \\ -\frac{\mu_a}{r^3} Z + \sum_{j=1}^{NP_j} a_P|_{z_j} + a_{srp}|_z \end{bmatrix} = \begin{bmatrix} F_1 \\ F_2 \\ F_3 \\ F_4 \\ F_5 \\ F_6 \end{bmatrix} \tag{57}$$

where μ_a is the gravity constant of Ryugu. The 3rd body acceleration is given by:

$$\boldsymbol{a}_{Pj} = -\mu_{Pj} \left(\frac{\boldsymbol{\Delta}}{\Delta^3} + \frac{\boldsymbol{d}}{d^3} \right), \tag{58}$$

with $\boldsymbol{\Delta} = \boldsymbol{r} - \boldsymbol{d}$ where $\boldsymbol{r}$ is the spacecraft distance from Ryugu and $\boldsymbol{d}$ is the distance of the perturbing body (Pj) with Ryugu. For a non-diffusive flat surface with Earth-pointing orientation, the SRP acceleration is given by:

$$\boldsymbol{a}_{srp} = -\frac{K}{r_{ls}^2} \cos\theta \left((1-\epsilon) \frac{\boldsymbol{r}_{ls}}{r_{ls}} + 2\epsilon \cos\theta \hat{\boldsymbol{n}} \right), \tag{59}$$

where the normal vector ($\hat{\boldsymbol{n}}$) is Earth-pointing thus:

$$\hat{\boldsymbol{n}} = \frac{\boldsymbol{r}_{Earth}}{r_{Earth}}, \tag{60}$$

and

$$\cos\theta = \frac{\boldsymbol{r}_{ls} \cdot \boldsymbol{r}_{Earth}}{r_{ls} r_{Earth}}. \tag{61}$$

K is defined as:

$$K = \frac{P_0}{c} \frac{A_{sc}}{m_{sc}} \text{AU}^2. \tag{62}$$

The coefficients and the properties of the spacecraft in Eq. (62) are given in Sect. 3.

Note that $\epsilon = C_r - 1$ is the reflectivity (0 complete absorption or 1 complete specular reflection) and $\boldsymbol{r}_{ls}$ is the Sun-Spacecraft distance where the vector is pointing toward the Sun. ϵ is a direct function of the reflectively coefficient C_r. $\boldsymbol{r}_{Earth}$ is the Ryugu-Earth distance where the vector is pointing toward the Earth. If the diffusion term, ρ_d, is neglected, the absorption term is $\rho_a = 1 - \rho_s$ with $C_r = 1 + \rho_s$. We renamed specular reflection term, ρ_s, as ϵ. Equation (59) is particularly useful for orbit determination where the SRP acceleration is a simple function of the C_r parameter. Therefore, Eq. (59) is a preferable SRP acceleration formula when C_r is a consider parameter (Montenbruck and Gill 2005).

References

E. Belbruno, M. Gidea, F. Topputo, Weak stability boundary and invariant manifolds. SIAM J. Appl. Dyn. Syst. **9**, 1061–1089 (2010). https://doi.org/10.1137/090780638

E. Canalias, J.J. Masdemont, Eclipse avoidance for lissajous orbits using invariant manifold, in *Proceedings of the 55th IAC*, 4–8 Oct. 2004, Vancouver, British, Columbia, Canada IAC-04-A.6.07 (2004)

A. Farres, A. Jorba, J. Mondelo, B. Villac, Periodic motion for an imperfect solar sail near an asteroid, in *Advances in Solar Sailing* (2013). https://doi.org/10.1007/978-3-642-34907-2_53

S.C. Gordon, Orbit determination error analysis and station-keeping for libration point trajectories. PhD Dissertation, Purdue University (1991)

W. Koon, M. Lo, J. Marsden, S. Ross, Low energy transfer to the moon. Celest. Mech. Dyn. Astron. **81**, 63–73 (2001). https://doi.org/10.1023/A:1013359120468

D. Lauretta, S. Balram-Knutson, E. Beshore, W. Boynton, C. dAubigny, D. DellaGiustina, H. Enos, D. Gholish, C. Hergenrother, E. Howell, C. Johnson, E. Morton, M. Nolan, B. Rizk, H. Roper, A. Bartels, B. Bos, J. Dworkin, D. Highsmith, S. Sandford, OSIRIS-REx: sample return from asteroid (101955) Bennu. Space Sci. Rev. (2017). https://doi.org/10.1007/s11214-017-0405-1

O. Montenbruck, E. Gill, *Satellite Orbits Model, Methods and Applications* (Springer, Berlin, 2005)

D. Morabito, S. Shambayati, S. Finley, D. Fort, The Cassini May 2000 solar conjunction. IEEE Trans. Antennas Propag. **51**, 201–219 (2003). https://doi.org/10.1109/TAP.2003.809055

T. Morley, F. Budnik, Effects on spacecraft radiometric data at superior solar conjunction, in *20th International Symposium on Space Flight Dynamics*, 24–28 September, Annapolis, United States ISSFD (2007)

Y. Qi, S. Xu, R. Qi, Gravitational lunar capture based on bicircular model in restricted four body problem. Celest. Mech. Dyn. Astron. **120**, 1–17 (2014). https://doi.org/10.1007/s10569-014-9554-7

C. Renaultand, D. Scheeres, Statistical analysis of control maneuvers in unstable orbital environments. J. Guid. Control Dyn. **26**, 758–769 (2003). https://doi.org/10.2514/2.5110

S. Soldini, H. Takeuchi, S. Taniguchi, S. Kikuchi, Y. Takei, G. Ono, M. Nakano, T. Ohnishi, T. Saiki, Y. Tsuda, F. Terui, N. Ogawa, Y. Mimasu, T. Takahashi, A. Fujii, S. Nakazawa, K. Yoshikawa, Y. Oki, C. Hirose, H. Sawada, T. Yamaguchi, M. Yoshikawa, Hayabusa2's superior solar conjunction mission operations: planning and post-operation results. Astrodyn. J. **4** (2020, in press)

S. Takahashi, D. Scheeres, Effect of shifted origin on the J2 perturbed terminator orbit (2019)

B.D. Tapley, B.E. Schutz, G.H. Born, *Satellite Orbit Determination* (Elsevier, London, 2004)

M. Taylor, N. Altobelli, B. Buratti, M. Choukroun, The Rosetta mission orbiter science overview: the comet phase. Philos. Trans. R. Soc. A, Math. Phys. Eng. Sci. **375**, 20160262 (2017). https://doi.org/10.1098/rsta.2016.0262

Y. Tsuda, M. Yoshikawa, M. Abe, H. Minamino, S. Nakazawa, System design of the Hayabusa2 – asteroid sample return mission to 1999 JU3. Acta Astronaut. **91**, 356–362 (2013)

K. Uesugi, H. Matsuo, J. Kawaguchi, T. Hayashi, Japanese first double lunar swingby mission "Hiten". Acta Astronaut. **25**, 347–355 (1991). https://doi.org/10.1016/0094-5765(91)90014-V

S.W. Wagner, t.D. Goodson, Execution error modelling and analysis of the Cassini-Huygens spacecraft through 2007, in *Proceedings of the AAS/AIAA Space Flight Mechanics Meeting*. Galveston, Texas AAS 08-113 (2008)

S.i. Watanabe, Y. Tsuda, M. Yoshikawa, S. Tanaka, T. Saiki, S. Nakazawa, Hayabusa2 mission overview. Space Sci. Rev. **208**, 1–14 (2017). https://doi.org/10.1007/s11214-017-0377-1

S. Watanabe, M. Hirabayashi, N. Hirata, R. Noguchi, Y. Shimaki, H. Ikeda, E. Tatsumi, M. Yoshikawa, S. Kikuchi, H. Yabuta, T. Nakamura, S. Tachibana, Y. Ishihara, T. Morota, K. Kitazato, N. Sakatani, K. Matsumoto, K. Wada, H. Senshu, C. Honda, T. Michikami, H. Takeuchi, T. Kouyama, R. Honda, S. Kameda, T. Fuse, H. Miyamoto, G. Komatsu, S. Sugita, T. Okada, N. Namiki, M. Arakawa, M. Ishiguro, M. Abe, R. Gaskell, E. Palmer, O.S. Barnouin, P. Michel, A.S. French, J.W. McMahon, D.J. Scheeres, P.A. Abell, Y. Yamamoto, S. Tanaka, K. Shirai, M. Matsuoka, M. Yamada, Y. Yokota, H. Suzuki, K. Yoshioka, Y. Cho, S. Tanaka, N. Nishikawa, T. Sugiyama, H. Kikuchi, R. Hemmi, T. Yamaguchi, N. Ogawa, G. Ono, Y. Mimasu, K. Yoshikawa, T. Takahashi, Y. Takei, A. Fujii, C. Hirose, T. Iwata, M. Hayakawa, S. Hosoda, O. Mori, H. Sawada, T. Shimada, S. Soldini, H. Yano, R. Tsukizaki, M. Ozaki, Y. Iijima, K. Ogawa, M. Fujimoto, T.M. Ho, A. Moussi, R. Jaumann, J.P. Bibring, C. Krause, F. Terui, T. Saiki, S. Nakazawa, Y. Tsuda, Hayabusa2 observations of the top-shape carbonaceous asteroid 162173 Ryugu. Science **364**(6437), 268–272 (2019). https://doi.org/10.1126/science.aav8032

M. Yoshikawa, H. Yano, J. Kawaguchi, A. Fujiwara, M. Abe, T. Iwata, S. Tanaka, O. Mori, T. Yoshimitsu, Y. Takagi, H. Demura, T. Noguchi, H. Miyamoto, Technologies for future asteroid exploration: what we learned from Hayabusa mission. LPI Contrib. **1325**, 81 (2013)